JPL Publication 95-1, Vol. 3

Summaries of the Fifth Annual JPL Airborne Earth Science Workshop January 23–26, 1995

Volume 3. AIRSAR Workshop

Jakob van Zyl
Editor

January 23, 1995

National Aeronautics and
Space Administration

Jet Propulsion Laboratory
California Institute of Technology
Pasadena, California

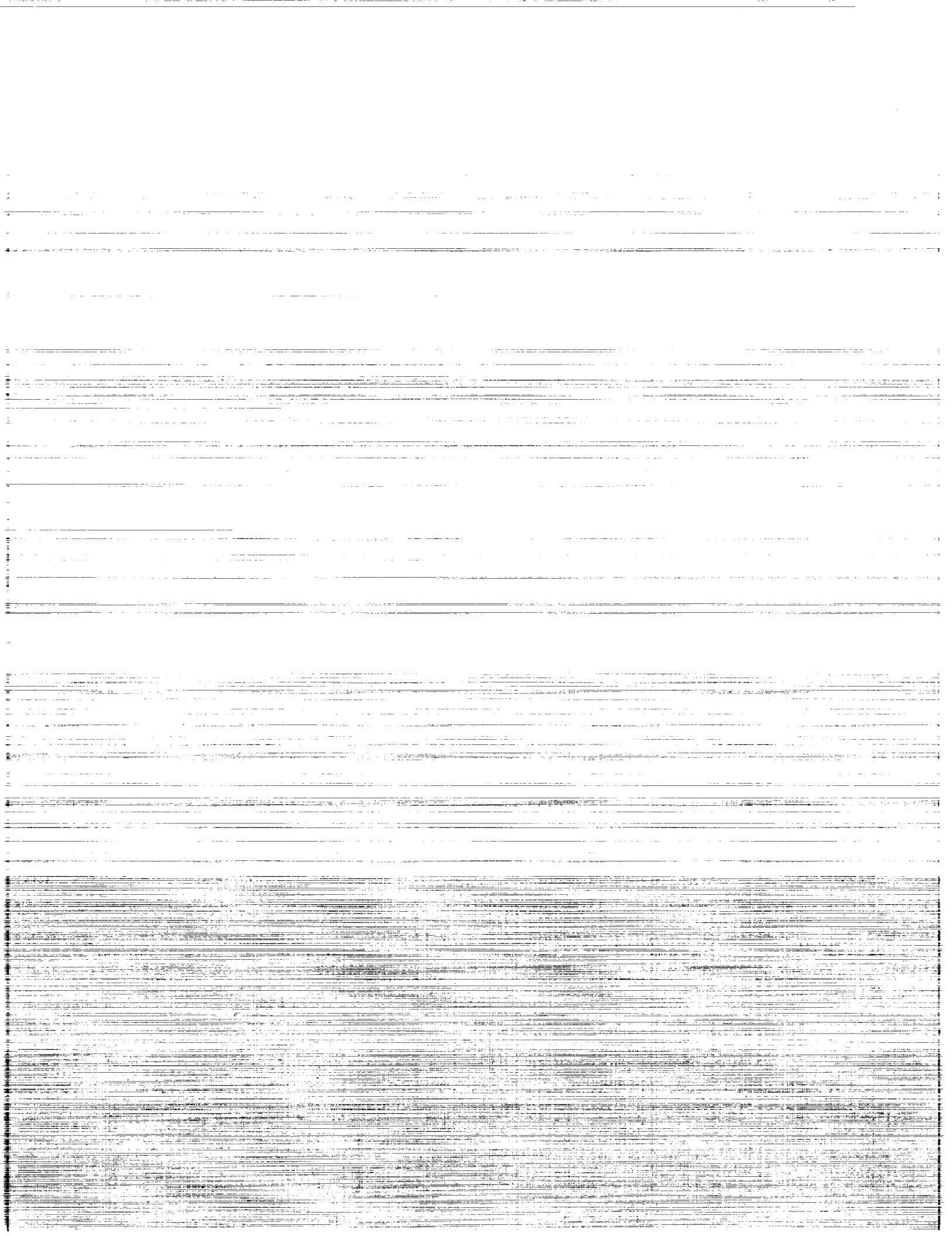

ABSTRACT

This publication contains the summaries for the Fifth Annual JPL Airborne Earth Science Workshop, held in Pasadena, California, on January 23–26, 1995. The main workshop is divided into three smaller workshops as follows:

- The Airborne Visible/Infrared Imaging Spectrometer (AVIRIS) workshop, on January 23–24. The summaries for this workshop appear in Volume 1.

- The Airborne Synthetic Aperture Radar (AIRSAR) workshop, on January 25–26. The summaries for this workshop appear in Volume 3.

- The Thermal Infrared Multispectral Scanner (TIMS) workshop, on January 26. The summaries for this workshop appear in Volume 2.

FOREWORD

In two of the papers for the AIRSAR Workshop, reference is made to color slides. A packet containing these slides was supplied at the time of the initial distribution of this volume.

Volume 1: AVIRIS Workshop

Volume 2: TIMS Workshop

Volume 3: AIRSAR Workshop

NEW OBSERVATIONS OF BOLIVIAN WIND STREAKS BY JPL AIRBORNE SAR; PRELIMINARY RESULTS

Dan G. Blumberg and Ronald Greeley

Department of Geology, Box 871404,
Arizona State University, Tempe Arizona 85287-1404.
e-mail Blumberg@ASUIP2.SPAN.NASA.GOV

1. INTRODUCTION

In 1993 NASA's Jet Propulsion Laboratory Airborne Synthetic Aperture Radar system (AIRSAR) was deployed to South America to collect multi-parameter radar data over pre-selected targets. Among the sites targeted was a series of wind streaks located in the Altiplano of Bolivia. The objective of this investigation is to study the effect of wavelength, polarization, and incidence angle on the visibility of wind streaks in radar data. Because this is a preliminary evaluation of the recently acquired data we will focus on one scene and, thus, only on the effects of wavelength and polarization. Wind streaks provide information on the near-surface prevailing winds and on the abundance of wind-erodible material, such as sand. The potential for a free-flyer radar system that could provide global radar images in multiple wavelengths, polarizations, and incidence angles requires definition of system parameters for mission planning. Furthermore, thousands of wind streaks were mapped from Magellan radar images of Venus (Greeley et al. 1992); their interpretation requires an understanding of the interaction of radar with wind streaks and the surrounding terrain. Our experiment was conducted on wind streaks in the Altiplano of Bolivia to address these issues.

The Altiplano is a continental basin with an average elevation of ~ 4000 m lying between the Eastern and Western Cordillera of the Andes. The geomorphology of the Altiplano (Ahlfeld, 1972) exhibits sand dunes, sand sheets, alluvium, and sediments deposited in glacial lakes. Aerial photographs of the Altiplano show that the predominant aeolian features are sand sheets and dunes. These features align with the prevailing westerly wind direction. For the deployment of AIRSAR, we targeted a series of wind streaks downwind of the volcano Cerro Quisharo. These streaks were first identified as radar visible by Greeley et al. (1989) following the first Shuttle Imaging Radar experiment (SIR-A; Elachi et al., 1982). These streaks emanate from small hills eastward, where they merge with the alluvium of the Rio Cosapa. The aeolian sediments consist primarily of quartz and pumice originating in alluvium and the volcanoes located west of the site.

2. DATA

The data used for this report were collected on 02 June 1993, as quad-polarized SAR data in C, L, and P wavelengths (λ=5.6, λ=24, and λ=68 cm respectively) stored as a compressed Stokes matrix (CM-4130). The resolution of the data is 8.27 m in azimuth and 6.66 m in range; the flight azimuth was 228 degrees. These data were calibrated by JPL and decompressed at Arizona State University on a VAX/VMS system to produce nine multilook ground-detected images (C, L, and P bands and HH, VV, and HV polarizations), with the scene centered at 18°27'S, 68°30.5'W. Figure 1 shows the L-band V V data used in this study.

3. ANALYSIS

3.1 Wavelength

Previous studies of radar visible wind streaks were conducted with SIR-A (Greeley et al. 1989) and Magellan data (Greeley et al. 1992). These were single wavelength and polarization systems. McCauley et al. (1982) demonstrated that radar energy can penetrate loose, dry, unvegetated sand mantles to a depth of a few meters below the surface. The depth of penetration increases as a function of wavelength, as reviewed by Elachi (1987). Under these circumstances, it was reasonable to anticipate that the longer wavelengths of AIRSAR would reveal less of the wind streaks than the shorter bands due to reflection from the substrate. However, in the Bolivian scene the longer wavelengths tend to reveal more of the wind streak than the shorter wavelength. We propose three mechanisms that could explain this apparent anomaly: 1) if there is a relatively thin sand mantle over the area, there would be more contrast between the streak (with the thicker mantle) and the surrounding terrain in the longer wavelengths (assuming that even in the long wavelengths, the energy does not penetrate down to to the substrate). 2) vegetation; the longer wavelengths could penetrate the surface and interact with root structures more than the shorter wavelengths, as shown by Greeley and Blumberg (submitted); thus, if there is more vegetation in the surrounding terrain than on the streaks, there would be a higher contrast between the streaks and the surroundings; 3) if there is very low vegetation on the east part of the streaks (the area less visible in C-band), volume scattering will occur only at $\lambda = 5.6$ cm within the canopy layer.

Most of the plains are characterized by an abundance of clusters of paja brava (small bushes) and thola (clump grass) spaced less than 2 m apart, coppice dunes (small sand mounds located around plants) spaced 5 to 20 m apart, and active windblown sand. Thus, it is reasonable that C-band would interact more with the vegetation than the L- and P-bands. Using a radar classification algorithm for detecting biomass (Freeman et al., 1993) we find that 62% of the surface is classified as low vegetation, with the remainder being free of vegetation. This supports the possibility that there would be more interaction with C-band than L- and P-bands. Moreover, coppice dunes do not tend to be very deep and C-band energy would probably reflect away from the radar antenna (off the sand) whereas L- and P-bands would penetrate and scatter off the substrate. Depending on the thickness of the material in the wind streaks, which is unknown at this time, L- and P- bands would probably not penetrate through the streaks to the substrate. These factors would contribute to less contrast in the shorter wavelength than in the longer wavelengths.

3.2 Polarization

The effect of polarization in wind streak visibility was tested using both raw-calibrated data and enhanced images. Preliminary analysis shows that like-polarized channels tend to show more of the wind streaks than the cross-polarized data for the shorter wavelengths. Among these, HH enhances the visibility of the streaks slightly in comparison to VV. This may be due to the presence of aeolian ripples on the streak that interact more with the horizontal wave than with the vertical wave (the height of the ripples is significantly less than the wavelength). However, in P-band the streaks are visible independent of polarization, suggesting that ripples are smooth to both the vertical and horizontal energy at this wavelength.

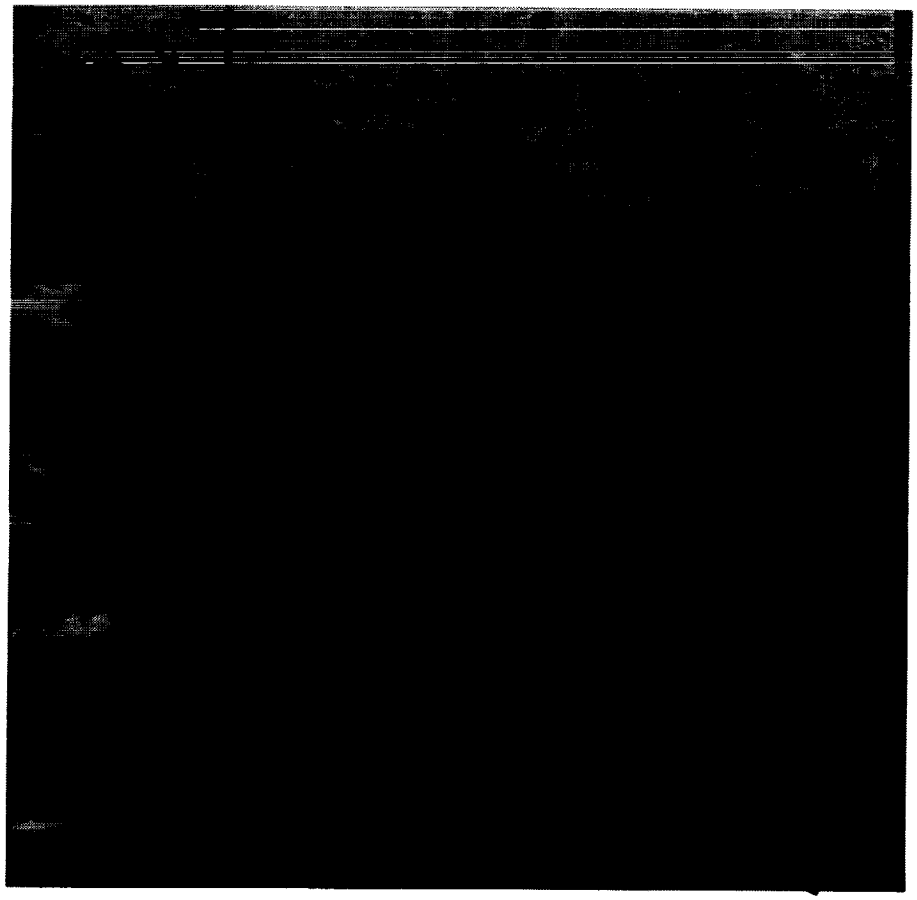

Figure 1. AIRSAR L-band vertical transmit and receive (V V) image of a series of wind streaks in the Bolivian Altiplano located downwind of the volcano Cerro Quisharo. Solid black arrows point to radar-visible wind streaks. Dunes (noted by open arrows) are visible in the AIRSAR images. The streaks provide information about near-surface winds and abundance of wind-erodible materials such as sand. The radar illumination is from top to bottom and flight azimuth is 228°. Image is centered at 18°27'S, 68°30.5'W. ASU - IPF Frame 963; CM4130.

3.3 Dunes

Greeley et al. (1989) showed that a single barchan dune could be detected within the streak in the SIR-A image. However, they noted that without prior knowledge of the existence of the dune, it probably would not have been found. The dune they observed was some 200 m across and 200 m long. The added resolution of AIRSAR over the 40 m resolution of SIR-A data, make this and additional dunes clearly visible as seen in Figure 1 (dunes noted by open arrows).

4. CONCLUSIONS AND FUTURE WORK

1. Preliminary results show that the visibility of wind streaks increases with the wavelength. However, this may not be the case in the absence of vegetation and this result needs to be tested.

2. We find that like-polarized channels are preferential for viewing wind streaks. We plan to test this result and determine if it results from local features such as ripples and vegetation. This will be done by selecting parts of streaks that are free of vegetation and by the use of other look angles to reduce the ripple affect.

3. Future work will include an analysis on the effect of incidence angle on the visibility of the streaks.

5. REFERENCES

Ahlfeld F., 1972, "*Geologia de Bolivia*" La Paz, Los Amigos del Libro, pp. 190.

Elachi C. et al., 1982, "Shuttle Imaging Radar.", *Science*, 218, pp. 966-1003.

Elachi C., 1987, "*Spaceborne Radar Remote Sensing; Applications and Techniques.*", IEEE Press, pp. 255.

Freeman A., B. Chapman, and M. Alves, 1993, "*MAPVEG Software Users' Guide.*", JPL Document D-11254, pp. 46.

Greeley and Blumberg. "Preliminary Analysis of Shuttle Radar Laboratory (SRL-1)Data to Study Aeolian Features and Processes.", *IEEE Trans. Geos. Remot. Sens.*, Submitted.

Greeley R., P. Christensen, and R. Carrasco, 1989, "Shuttle Radar Images of Wind Streaks in the Altiplano, Bolivia." *Geology*, 17, pp. 665-668.

Greeley, R., R.E. Arvidson, C. Elachi, M.A. Geringer, J.J. Plaut, R.S. Saunders, G. Schubert, E.R. Stofan, E.J.P. Thouvenot, S.D. Wall, and C.M. Weitz, 1992, "Aeolian Features on Venus: Preliminary Magellan Results." *JGR* 97 E8, pp. 13319-13345.

MEASURING SOIL MOISTURE WITH IMAGING RADARS

Pascale C. Dubois(*), Jakob van Zyl(*) and Ted Engman (**)
(*): Jet Propulsion Laboratory, California Institute of Technology
4800 Oak Grove Drive, Pasadena CA 91109
(**) NASA Goddard Space Flight Center
E-mail: pascale@blacks.jpl.nasa.gov Ph: (818) 354-0497

1. INTRODUCTION

An empirical model was developed to infer soil moisture and surface roughness from radar data. The accuracy of the inversion technique is assessed by comparing soil moisture obtained with the inversion technique to *in situ* measurements. The effect of vegetation on the inversion is studied and a method to eliminate the areas where vegetation impairs the algorithm is described.

2. EXPERIMENTAL DATA AND MODEL DESCRIPTION

Two sources of experimental data were used in the derivation of the empirical model. The University of Michigan's LCX POLARSCAT is a truck-mounted network-analyzer-based scatterometer operating at three frequencies: 1.25, 4.75 and 9.5 GHz. The POLARSCAT data set (Oh et al., 1992) used in this study includes the co- and cross-polarized (hh, vv and hv) backscatters for four surfaces. The RASAM radar developed by the University of Bern, Switzerland is a truck-mounted radiometer-scatterometer with the scatterometer system operating at six frequencies between 2.5 GHz and 11 GHz. A complete description of the instrument can be found in (Wegmuller, 1993). The RASAM data set includes measurements of the hh, vv, hv and vh-polarized backscattering coefficients over a variety of surfaces.

Using these two data sets, the hh-polarized and vv-polarized backscattering coefficients σ^0_{hh} and σ^0_{vv} were empirically found to follow these two equations:

$$\sigma^0_{hh} = 10^{-2.75}\frac{\cos\theta^{1.5}}{\sin\theta^5}10^{0.28\varepsilon\tan\theta}(kh\sin\theta)^{1.4}\lambda^{0.7}$$

$$\sigma^0_{vv} = 10^{-2.35}\frac{\cos\theta^{3}}{\sin\theta^3}10^{0.46\varepsilon\tan\theta}(kh\sin\theta)^{1.1}\lambda^{0.7} \qquad (1)$$

where θ is the incidence angle, ε is the real part of the dielectric constant, h is the RMS height of the surface, k is the wave number and λ is the wavelength in cm.

The general backscatter behavior with roughness and dielectric constant is similar to the trend predicted by the small perturbation model and the physical optics model (Ulaby et al., 1986). The backscatters decrease with increasing incidence angle and with decreasing roughness. Restricting the validity of the model to $kh \le 2.5$ and $\theta \ge 30°$ will insure that the $\sigma^0_{hh}/\sigma^0_{vv}$ ratio is always less than 1. We note that the roughness of the natural surfaces that the algorithm is applied to rarely exceeds $kh = 2.5$ (corresponding for L-band to an RMS height of 10 cm).

3. EFFECTS OF VEGETATION AND CALIBRATION

The inversion relies on the co-polarized channels and does not use the cross-polarized channels. This has several advantages. The first advantage is that the co-polarized channels can be calibrated directly with passive targets like corner reflectors.

The cross-polarized channel calibration is usually derived from measurements made on the co-polarized channels and as a result is less accurate than the calibration made on the co-polarized channels. The second advantage is the normally higher signal-to-noise ratio in the co-polarized channels than in the cross-polarized channels. Finally, the third advantage is that vegetation is known to have a relatively strong effect on the cross-polarized channel (Le Toan et al., 1992). It can therefore be expected that an inversion algorithm relying on the co-polarized channels will be more robust to the presence of vegetation than one relying on both the cross- and the co-polarized channels. Nevertheless, for a significant amount of vegetation, the algorithm will overestimate surface roughness and underestimate soil moisture.

Active microwave sensors have been shown to be good discriminators for biomass (Le Toan et al., 1992). This capability can be used to select the areas with low vegetation cover where the inversion can be applied. The L-band $\sigma^0_{hv}/\sigma^0_{vv}$ ratio image acquired over Chickasha, Oklahoma was compared to a SPOT-derived Normalized Difference Vegetation Index (NDVI) image (Tucker, 1979) over the same area. Overall, a pixel-to-pixel comparison between the two indices provides the regression curve. This curve shows that the L-band parameter is positively correlated to the NDVI. We found that masking out the areas for which the L-band $\sigma^0_{hv}/\sigma^0_{vv}$ ratio is greater than -11 dB, results in a reliable soil moisture estimate. The -11 dB $\sigma^0_{hv}/\sigma^0_{vv}$ ratio corresponds to NDVI of around 0.4.

The study showed that a desired 4% accuracy in soil moisture estimate requires a .5 dB accuracy of the relative calibration and a 2 dB accuracy in the absolute calibration. Both requirements are met by both the AIRSAR L-band and the SIR-C sensor. It should therefore be possible to derive accurate soil moisture maps for the data provided operationally by these sensors.

4. SAR DATA INVERSION

The inversion technique was first applied to Washita'92 AIRSAR data. The experiment followed a period of heavy rain so that the conditions on June 10, 1992 were very wet with standing water and saturated soils fairly common. No further rain fell during the next nine days and we were able to follow a drying pattern. The area covered in the AIRSAR Workshop Slide 1 is around 8 km by 10 km. It was imaged by the AIRSAR system on six different days between June 10 and June 18, 1992. An L-band hh image is displayed at the lower right corner. The AG002 bare field which was extensively studied is outlined in the image. The other six images were obtained by inverting the L-band data acquired on the corresponding days. The dielectric constant maps were translated into soil moisture maps using the Hallikainen empirical curves (Hallikainen et al., 1985). The black areas in the soil moisture maps indicate areas where the vegetation cover is too thick for the inversion to be reliable. The scatter plot is a comparison between the *in-situ* measurements and the estimated values of soil moisture over the AG002 field. The RMS error of the soil moisture estimate is 1.6 %. The RMS height maps corresponding to the six data takes are very similar and indicate no trend in roughness changes. The quantitative results are presented in Table 1.

Washita'94 was an aircraft and shuttle experiment that occurred between April 9 and April 18 in which the shuttle took data on April 11 through 17 and the AIRSAR on April 10 and 11. Two of the sampled fields where data are already available are in the radar scene and meet the low vegetation criteria described earlier. The results from the inversion are included in Table 1 for both SIR-C and for AIRSAR.

The soil moisture inversion algorithm was also applied to an AIRSAR data set acquired over Spain in the summer of '91 during the EFEDA campaign (Bolle et al., 1992). Three of the sampled fields are in the radar scene and meet the low vegetation

criteria described earlier. The results from the inversion are included in Table 1. Over all the areas where SAR data and ground truth measurements are available, the RMS error in soil moisture is 3.5% (see Table 1 and Figure 1).

5. CONCLUSIONS

We presented an empirical algorithm to infer soil moisture from imaging radar data over bare surfaces using two co-polarized radar cross-section measurements. The algorithm was developed with scatterometer data, and tested with several data sets acquired with the AIRSAR system; we also presented the first soil moisture images derived from spaceborne SIR-C SAR data. A comparison with in situ data shows that the algorithm infers soil moisture with an accuracy of better than 4 %. Best results are achieved when the surface roughness is such that $kh < 2.5$ (10 cm RMS height for L-band) and the incidence angle is larger than 30 degrees. We also quantified the calibration requirements of the algorithm and established that current operational multipolarization SAR systems such as AIRSAR and SIR-C routinely deliver images that meet or exceed these calibration requirements. We also presented evidence that the ratio of the cross-polarized return to the like-polarized return could be used to decide which areas the algorithm can be applied to and showed that this ratio was positively correlated with NDVI.

Scene	Sensor	Data Take	Date	Field ID	Mv Msd [%]	Mv Est. [%]	h Msd (cm)	h Est. (cm)
CHICKASHA	AIRSAR	3902	6/10/92	AG002	28.7	29.2	1.19	1.18
CHICKASHA	AIRSAR	3664	6/12/92	AG002	22.4	21.2	1.19	1.35
CHICKASHA	AIRSAR	3359	6/13/92	AG002	24.1	23.5	1.19	1.09
CHICKASHA	AIRSAR	3875	6/14/92	AG002	18.1	19.4	1.19	1.19
CHICKASHA	AIRSAR	3883	6/16/92	AG002	13.6	17	1.19	1.24
CHICKASHA	AIRSAR	3360	6/18/92	AG002	11.6	12.1	1.19	1.45
CHICKASHA	AIRSAR	4040	6/17/92	AG002	17.5	18.5	1.19	1.45
CHICKASHA	AIRSAR	4041	6/13/92	AG002	24.1	27.4	1.19	1.38
CHICKASHA	AIRSAR	Mosaic	6/13/92	RG148	27.6	30.6		
CHICKASHA	AIRSAR	Mosaic	6/13/92	RG131	29.2	34.5		
CHICKASHA	AIRSAR	4254	4/12/94	Field 12	18.4	24.5		1.58
CHICKASHA	AIRSAR	4254	4/12/94	Field 15	24.8	21.8		0.86
EFEDA	AIRSAR	3146	6/13/90	Field 2	3.4	6.9	1.41	1.34
EFEDA	AIRSAR	3146	6/13/90	Field 4	30.6	22.8	0.6	0.9
EFEDA	AIRSAR	3146	6/13/90	Field 5	18.6	18.2	1.79	0.8
CHICKASHA	SIR-C	10155	4/12/94	Field 12	18.4	20.2		1.2
CHICKASHA	SIR-C	10155	4/12/94	Field 15	24.8	30.3		1.24
CHICKASHA	SIR-C	10158	4/15/94	Field 12	9.9	12.5		2
CHICKASHA	SIR-C	10158	4/15/94	Field 15	12.5	11.8		1.5
RMS ERROR						3.3		0.34

Table 1: Comparison between in situ measurements and estimated values. Mv stands for volumetric soil moisture, h for the RMS height. Est. and Msd indicate the radar derived values and the ground truth measurements.

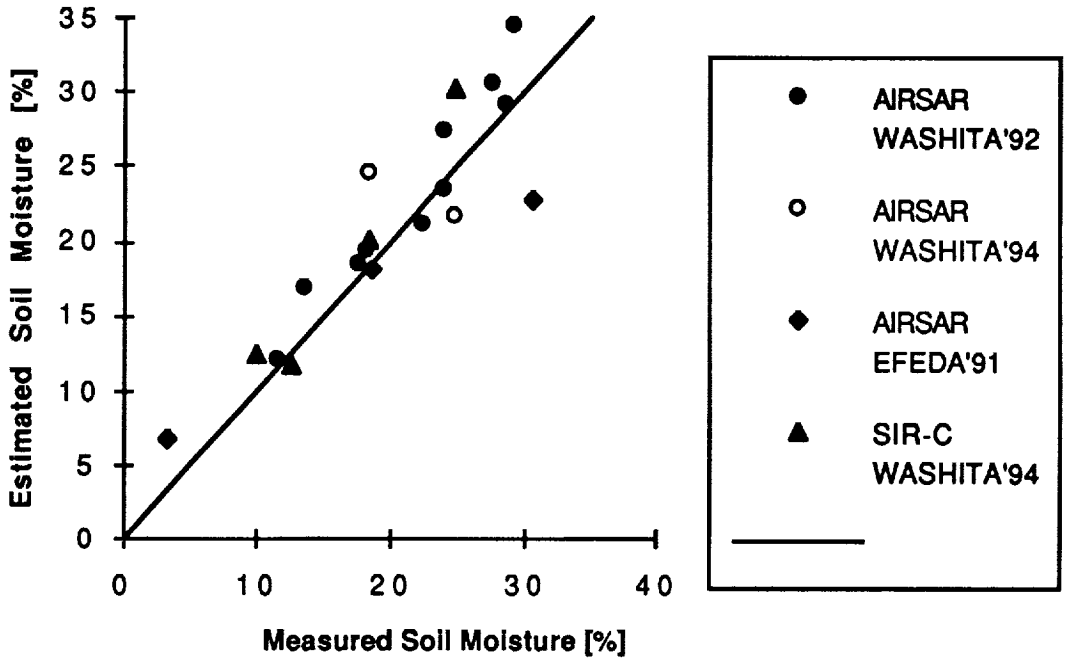

Figure 1: Radar derived soil moisture versus in situ measurements.

6. ACKNOWLEDGMENT

We would like to thank our colleagues from University of Michigan and University of Bern for sharing their scatterometer data and the corresponding ground truth with us. Our gratitude also goes to all the people involved in collecting the ground truth we used to validate this study. We would also like to acknowledge the help we received from Tom Jackson of the U.S. Department of Agriculture and his team. This work was performed at the Jet Propulsion Laboratory, California Institute of Technology under contract with the National Aeronautics and Space Administration.

7. REFERENCES

Bolle, H. J. and B. Streckenbach, 1992, " The ECHIVAL field experiment in a desertification-threatened area EFEDA, " First Annual Report to EC, published by the EFEDA-secretariat, Free University of Berlin, Berlin, Germany.

Hallikainen, M.T. , F. T. Ulaby, M. C. Dobson, M.A. El-Rayes and L. Wu, 1985, "Microwave dielectric behavior of wet soil - Part I: Empirical models and experimental observations," *IEEE Trans. Geosc. Remote Sensing*, vol. GE-23, pp. 25-34, 1985.

Oh, Y., K. Sarabandi and F. Ulaby, 1992, "An Empirical Model and an Inversion Technique for Radar Scattering from Bare Soil Surfaces," *IEEE Trans. on GRS*, vol. GE-30, No. 2.

Le Toan, T., A. Beaudoin and D. Guyon, 1992, "Relating forest biomass to SAR data," IEEE Transactions on Geoscience and Remote Sensing, Vol. 30, No. 2.

Tucker, C. J., 1979, "Red and photographic infrared combinations for monitoring vegetation," Remote Sensing of the Environment, vol. 8, pp. 127-150.

Ulaby, F.T., R. K. Moore, and A. K. Fung, 1986, *Microwave Remote Sensing: Active and Passive*, vol. 3, From theory to Applications, pp. 1065-2162, Dedham, MA: Artech House.

Wegmuller, U., 1993, "Active and Passive Microwave Signature Catalogue on Bare Soil (2-12 GHz), " Institute of Applied Physics, University of Bern, Switzerland, 1993.

USE OF TOPSAR DIGITAL ELEVATION DATA TO DETERMINE THE 3-DIMENSIONAL SHAPE OF AN ALLUVIAL FAN

Tom G. Farr
Jet Propulsion Laboratory
California Institute of Technology
Pasadena, CA

Landforms in arid regions record the interplay between tectonic forces and climate. Alluvial fans are a common landform in desert regions where the rate of uplift is greater than weathering or sedimentation (Bull, 1991; Bull and McFadden, 1977). Changes in uplift rate or climatic conditions can lead to isolation of the currently forming fan surface through entrenchment and construction of another fan either further from the mountain front (decreased uplift or increased runoff) or closer to the mountain front (increased uplift or decreased runoff). Thus, many alluvial fans are made up of a mosaic of fan units of different age, some older than 1 million years. For this reason, determination of the stages of fan evolution can lead to a history of uplift and runoff.

In an attempt to separate the effects of tectonic (uplift) and climatic (weathering, runoff, sedimentation) processes on the shapes of alluvial fan units, a modified conic equation developed by Troeh (1965) was fitted to TOPSAR digital topographic data for the Trail Canyon alluvial fan in Death Valley, California. This allows parameters for the apex position, slope, and radial curvature to be compared with unit age.

Troeh's (1965) equation is given as:

$$Z = P + S\sqrt{(X-X_0)^2 + (Y-Y_0)^2} + L\{(X-X_0)^2 + (Y-Y_0)^2\}$$

where Z is the height at position X, Y; X_0, Y_0, and P are the coordinates of the cone apex; S is the slope at the apex; and L is the radial curvature. Note that the term containing L adds a radial curvature to the simple right-circular cone described by the rest of the equation.

Troeh (1965) accomplished his work with topographic contour maps. With the advent of modern digital computers and digital elevation models, his approach can now be taken further and used to compare the topographic attributes of many alluvial fans or individual fan units with their age, drainage basin size, relief, lithology, uplift rates, etc. Further, the original extent and volume may be estimated for fan units of which only remnants are exposed. The topographic signature of individual fan units will help in regional correlation of fan surfaces of similar age.

A variety of techniques have been used over the years to map the relative ages of alluvial fan surfaces in arid regions. Since suitable material for numerical age determination is scarce in these environments, the actual depositional history of few fans has been determined. Exceptions include the fans on the west side of Silver Lake (Wells et al., 1987) and on the west side of the Owens Valley (Gillespie, 1982). In addition, tentative age assignments for major units on the fans along the west side of Death Valley, mapped by Hunt and Mabey (1966),

have been made by Dorn (1988). These studies indicate that major pulses of fan aggradation are related to climatic changes that occur either during or at the close of major glaciations when rainfall and weathering processes are most conducive to the formation of debris flows and fluvial activity.

In order to characterize topographically the alluvial fan units mapped by Hunt and Mabey (1966), sufficient resolution is required to discriminate the individual units and sufficient coverage is required to provide enough points for a meaningful fit. Typical units, as mapped by Hunt and Mabey (1966) and by other students of alluvial fans (e.g. Hooke, 1972) are tens of m wide and cover in aggregate, at least in the case of the Trail Canyon fan, an area of several square km. Another requirement on the data to be used for 3-dimensional fitting is that the vertical errors in the data are smaller than the signal on the alluvial fans. On the Trail Canyon fan, relief differences between fan units are generally less than 5 m, while dissection within units typically ranges between 1 and 2 m.

There are several sources of digital topographic data that could be used for measurements of desert piedmont shapes. The most widely available data that most closely satisfy the above requirements are the U.S. Geological Survey's 7.5' Digital Elevation Models (DEM). The horizontal resolution (pixel size) of these data is 30 m and the vertical accuracy ranges between 7 and 15 m. These DEMs, however, are not available for large areas, including Death Valley. For this study, data from the NASA/JPL TOPSAR was used (Zebker et al., 1992; Evans et al., 1992). The spatial resolution of the TOPSAR data for Trail Canyon is 20 m. Analysis of TOPSAR data in control areas indicates that statistical errors in height are in the 1 m range, while systematic effects due to aircraft motion are in the 1-2 m range. Performance is best in areas of low relief and degrades slightly in the far range, as the signal to noise ratio decreases.

The results of the conic fits to individual units on the Trail Canyon fan show that the fan has changed shape over time. The causes of these changes may be climatic, tectonic, or a combination of the two. The fits show that older units are flatter at the cone apex and have less radial curvature, that the two younger units are entrenched into the fan head, and the youngest unit is depositing at the toe of the fan. These data can be used to make inferences about the processes that have formed and modified Trail Canyon fan. In particular, the similarity of the fan-unit shapes is probably a reflection of a consistent tectonic uplift rate since the deposition of the oldest unit.

In order to make more far-reaching conclusions, additional studies of other fans in Death Valley and in other desert basins need to be undertaken. Fan shapes need to be correlated to drainage-basin size, relief, lithology, etc. in order to separate the effects of climate and tectonic uplift. Comparing basins subjected to similar uplift rates, but with different basin geometries and lithologies will help isolate the climatic variable. Whereas, comparing basins with similar regional climate, and presumably paleoclimate, but with different uplift rates will help isolate the tectonic variable. In this way, comparative analysis of the three-dimensional shapes of alluvial fan units may be used in combination with field observations, aerial-photographic analyses, and remote sensing (Farr and Gillespie, 1984; Gillespie et al., 1984; Gillespie et al., 1986) for more precise mapping and regional correlation of alluvial fan units.

Acknowledgments

The research described in this report was carried out by the Jet Propulsion Laboratory, California Institute of Technology, under contract with the National Aeronautics and Space Administration.

References

Bull, W.B., 1991, *Geomorphic Responses to Climatic Change*, Oxford Univ. Press, New York, 326 pp.

Bull, W.B., L.D. McFadden, 1977, Tectonic geomorphology north and south of the Garlock Fault, California, in *Geomorphology in Arid Regions*, D.O. Doehring, ed., Proc. 8th Annual Geomorphology Symposium, SUNY Binghamton, p. 115-137.

Dorn, R.I., 1988, A rock-varnish interpretation of alluvial-fan development in Death Valley, California, National Geog. Res., v. 4, p. 56-73.

Evans, D.L., T.G. Farr, H.A. Zebker, J.J. van Zyl, P.J. Mouginis-Mark, 1992, Radar interferometry studies of the Earth's topography, Eos Trans. AGU, v. 73, p. 553-558.

Farr, T.G., A.R. Gillespie, 1984, Measurement of micro-relief on alluvial fans and its relation to age, lithology, and radar response, Geological Society of America Abs. with Prog., v. 16, p. 506.

Gillespie, A.R., 1982, Quaternary Glaciation and Tectonism in the Southeastern Sierra Nevada, Inyo County, California, unpublished PhD thesis, California Institute of Technology, Pasadena, CA, 695 pp.

Gillespie, A.R., E. Abbott, G. Hoover, 1986, Spectral basis for relative dating of granitic alluvial fans, Owens Valley, California, Geol. Soc. Amer. Abs. with Prog., v. 18, p. 614.

Gillespie, A.R., A.B. Kahle, F.D. Palluconi, 1984, Mapping alluvial fans in Death Valley, California, using multichannel thermal infrared images, Geophys. Res. Let., v. 11, p. 1153-1156.

Hooke, R. LeB., 1972, Geomorphic evidence for late-Wisconsin and Holocene tectonic deformation, Death Valley, California, Geol. Soc. Amer. Bull., v. 83, p. 2073-2098.

Hunt, C.B., D.R. Mabey, 1966, Stratigraphy and structure, Death Valley, California, U.S. Geol. Surv. Prof. Paper 494-A, 162 pp.

Troeh, F.R., 1965, Landform equations fitted to contour maps, Amer. Jour. Sci., v. 263, p. 616-627.

Wells, S.G., L.D. McFadden, J.C. Dohrenwend, 1987, Influence of late Quaternary climatic changes on geomorphic and pedogenic processes on a desert piedmont, eastern Mojave Desert, California, Quat. Res., v. 27, p. 130-146.

Zebker, H.A., S.N. Madsen, J. Martin, K.B. Wheeler, T. Miller, Y. Lou, G. Alberti, S. Vetrella, A. Cucci, 1992, The TOPSAR interferometric radar topographic mapping instrument, IEEE Trans. Geosci. Rem. Sens., v. 30, p. 933-940.

N95-33805

ACCURATE ESTIMATION OF σ^o USING AIRSAR DATA

Francesco Holecz * and Eric Rignot
Jet Propulsion Laboratory, California Institute of Technology,
4800 Oak Grove Drive, M/S 300-243, Pasadena CA 91109
FAX: 818 393 6943, E-mail: franci@blacks.jpl.nasa.gov
* on leave from Remote Sensing Laboratories, University of Zürich, Switzerland

1. INTRODUCTION

During recent years signature analysis, classification, and modeling of Synthetic Aperture Radar (SAR) data as well as estimation of geophysical parameters from SAR data have received a great deal of interest. An important requirement for the quantitative use of SAR data is the accurate estimation of the backscattering coefficient σ^o. In terrain with relief variations radar signals are distorted due to the projection of the scene topography into the slant range-Doppler plane. The effect of these variations is to change the physical size of the scattering area, leading to errors in the radar backscatter values and incidence angle. For this reason the local incidence angle, derived from sensor position and Digital Elevation Model (DEM) data must always be considered. Especially in the airborne case, the antenna gain pattern can be an additional source of radiometric error, because the radar look angle is not known precisely as a result of the the aircraft motions and the local surface topography. Consequently, radiometric distortions due to the antenna gain pattern must also be corrected for each resolution cell, by taking into account aircraft displacements (position and attitude) and position of the backscatter element, defined by the DEM data.

In this paper, a method to derive an accurate estimation of the backscattering coefficient using NASA/JPL AIRSAR data is presented. The results are evaluated in terms of geometric accuracy, radiometric variations of σ^o, and precision of the estimated forest biomass.

2. METHOD

From the radar equation for distributed targets it is known that the received power is modulated with the 2-way-antenna gain $G(\theta)^2$ and with the reciprocal value of $1/\sin\theta_i$, where θ_i is the local incidence angle. For each pixel these quantities are dependent on the radar look angle θ, the depression angle of the antenna, the sensor position and attitude, the position of the backscatter element, as well as on the processed pixel spacing in range and azimuth. Since SAR processing does not include topographic information, these two radiometric corrections are omitted during the processing step, and therefore they should be considered in a postprocessing step (van Zyl et al., 1993; Holecz et al., 1994). Figure 1 gives an overview of the required input data, and summarizes the various steps. The method is discussed in detail in Holecz et al. (1994). Note that geometric calibration does not include a geocoding of the image. It only considers the relationship between the sensor and each single backscatter element. This, of course, can be achieved even in the original image geometry without resampling the SAR data.

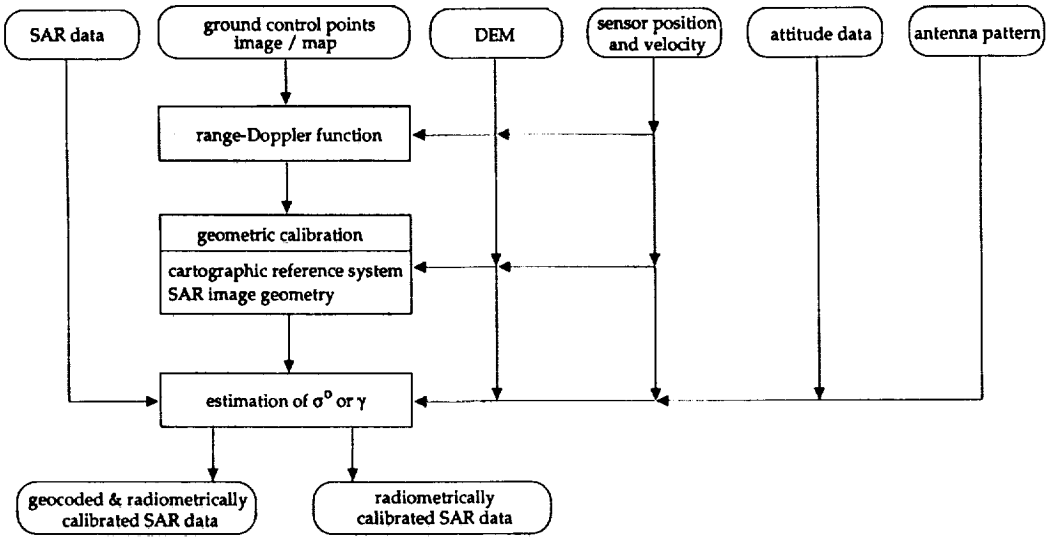

Figure 1: Derivation of the backscattering coefficient

3. DATA SETS

The SAR data used in this study were collected by the AIRSAR system on May 6 of 1991 over the hilly area (190 to 500 meters above mean sea level) of the Bonanza Creek Experimental Forest (64.75°N, -148°W), near Fairbanks, Alaska. The 16-look image covers an area of around 100 km^2.

One prerequisite is the availability of DEM. For the BCEF test site only 15 minute DEM data of the US Geological Survey are available. The data were transformed from the original geographic coordinate system into the Universal Transverse Mercator coordinate system (zone 6) and resampled to 12.5 meter grid size using a bilinear interpolator.

Further required data are position and attitude data of the platform. The NASA/ARC DC-8 aircraft is currently equipped with three operational navigation systems, namely the Data Aircraft and Distribution System (DADS), the Laser Reference System (LRS), and the Six Gun Global Positioning System (SG-GPS) (DC-8 ALEH, 1990). DADS data include yaw, pitch, roll, latitude, longitude, and altitude of the aircraft above the ground, while LRS measures yaw, pitch, roll, latitude, longitude, three-dimensional velocity vector, and track angle of the aircraft. The positioning data of the third system are stored in latitude, longitude, and altitude above sea level. DADS and SG-GPS are updated every second, while LRS updates every 0.02 second. The absolute positioning accuracy of DADS and SG-GPS is ±200 meters, while LRS can achieve a better accuracy. However, since LRS is not locked to other systems, it can drift significantly with time. Two new experimental systems are the Turbo-Rogue GPS (TR-GPS) and the Honeywell Inertial Navigation Unit (HW-INU) having an acquisition rate of 1 and 50 Hz, respectively. The positioning accuracy in real time of the TR-GPS corresponds to the SG-GPS, but in differential mode, it is in the order of ±10 cm. The data acquired by the HW-INU system achieve a positioning precision of ±3 meter and an attitude accuracy of ±1/1000 degree.

4. RESULTS

Figure 2 shows the P-band total power in slant range geometry and in UTM coordinate system (zone 6), respectively. As already mentioned radiometric errors due to the topographic effects and the aircraft displacements must be additionally considered. Therefore, the local incidence angle as well as the antenna gain pattern correction were calculated and shown in Figure 3 (a-d). Since these two corrections are carried out in the original SAR geometry (slant or ground range projection) and in the cartographic reference system, the backscattering coefficient can be derived in both reference systems.

What are the consequences of the topographic effects for the forest biomass estimation? It has already been noticed in Rignot et al. (1994) that DEM should be combined with the SAR data, in order to improve radar estimates of forest biomass in areas with topography. Here, we analyse these effects. The backscattering coefficients at P-band for HH, VV, and HV polarization are derived taking into account to the variations of local incidence angle as well as of the antenna gain pattern using the DEM data. The forest biomass, as shown in Figure 4, is then estimated with a regression curve applied to σ^0 of the three linear polarizations.

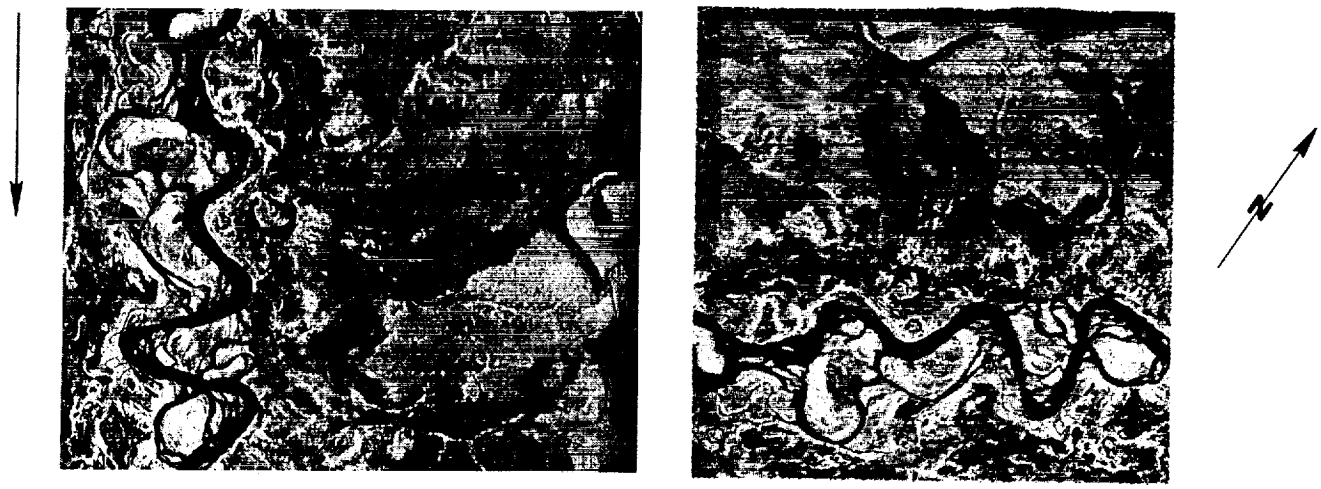

Figure 2: P-band total power in slant range geometry (left) and in UTM coordinate system (right)

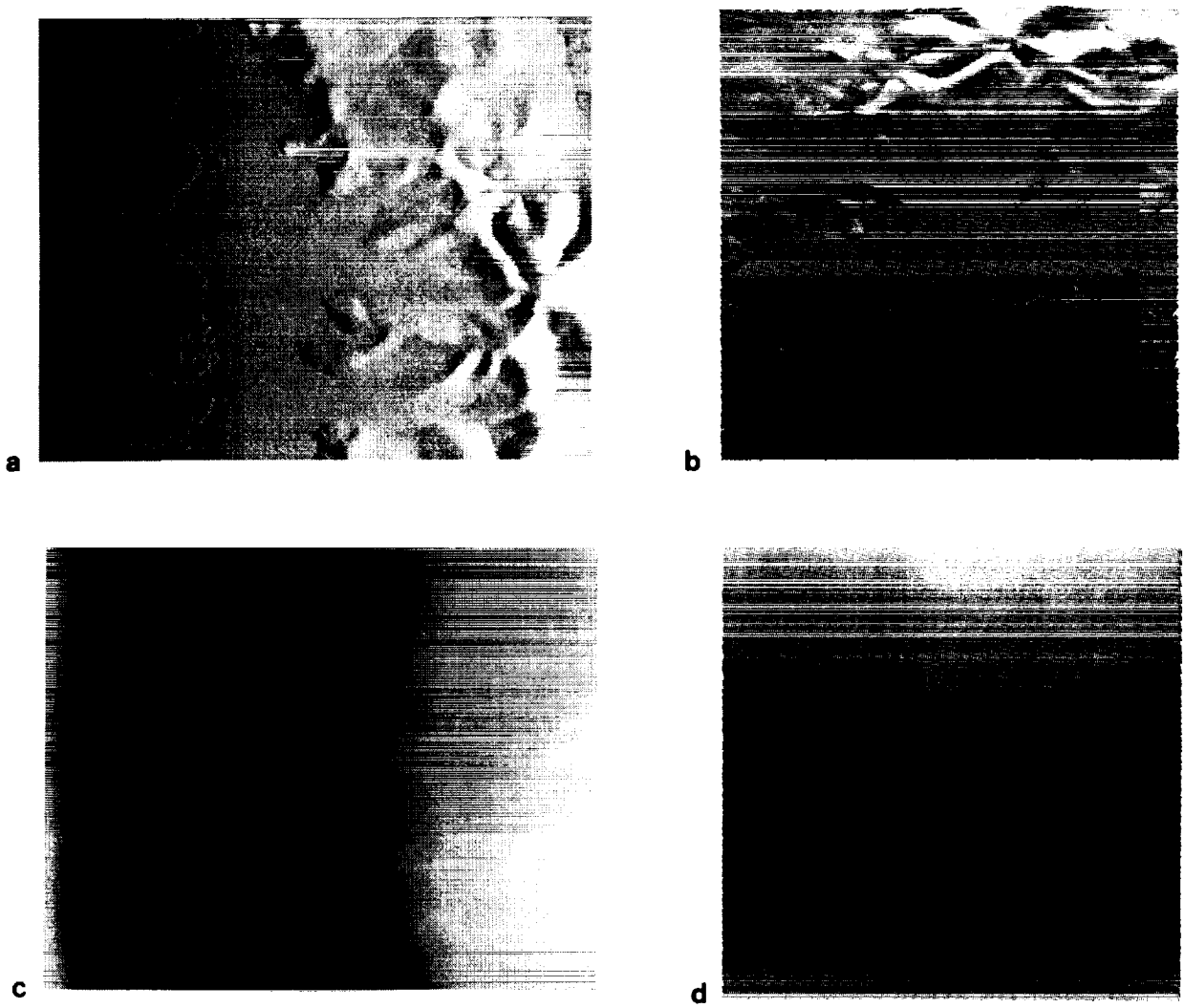

Figure 3: Local incidence angle in a) slant range geometry and b) in UTM coordinate system; Correction of antenna gain pattern at P-band HV in c) slant range and d) UTM coordinate system

Figure 4: Estimated forest biomass (metric tons/ha) using P-band data in slant range geometry

5. DISCUSSION OF THE RESULTS AND CONCLUSIONS

The presented results are discussed and evaluated in the following terms:

- **Geometric accuracy:** For an accurate estimation of the backscattering coefficient, flight path data (position and attitude), DEM, sensor and processor characteristics have been considered. This, of course, includes all the cartographic and geodetic transforms, as well as a range-Doppler approach (Meier et al., 1993). For the AIRSAR system the positioning data collected by the three operational navigation systems during this flight showed high inaccuracies. Only DADS data could be used, with an absolute positioning inaccuracy of about 1000 meters. However, using ground control points we achieved an average geometric accuracy of the geocoded image of ±30 meters (grid size of the DEM is 12.5 meters). These deviations are due to inaccuracies a) of the operational navigation system (relative inaccuracies), b) of the ground control points extracted from a 1:63,360 scale map, c) of the low resolution of the DEM data, and d) motion errors of the aircraft not considered during the SAR processing. It must be pointed out that some AIRSAR data acquired after 1993 have already been processed taking into account motion errors of the aircraft. Furthermore the accuracy of positioning and attitude data is being improved by using the two new experimental systems mentioned in section 3. Consequently, a geometric accuracy in the order of ±1 pixel is expected.
- **Radiometric variations of σ^o:** Even in a moderately hilly area as the BCEF test site, topographic effects on the radiometric calibration cannot be neglected. In fact, radiometric errors exceeding 3 dB in magnitude have been observed. The major contributions are due to the effects on the local incidence angle (up to 1.9 dB), but also local surface changes and variations of the roll angle on the antenna gain pattern correction caused radiometric errors up to 1.3 dB at P-band (HV 1.30, HH 1.25, VV 1.34). However, as already reported in Holecz et al. (1993), the quality of the DEM data strongly influences the radiometric calibration and therefore the accuracy of the backscattering coefficient. It has also to be noted that the topography in the SAR image is located in the far range part (see Figure 3a). Consequently, radiometric errors due to relief effects are relatively small, mainly because of the large radar look angle.
- **Accuracy of the estimated forest biomass:** In the biomass map shown in Figure 4 we estimated the radar-predicted values to be within 20% of actual values obtained using forest inventory and allometric equations (Rignot et al., 1994). However, this accuracy is only applicable to forest stands in the floodplains and in the south-, radar-facing, slopes in the upland forests. These stands are all imaged at an incidence angle of about 45 degrees. In the north-facing slopes, away from the radar, the radar underestimates the biomass because the incidence angle is several tens of degrees away from 45 degrees, and radar backscatter is not correctly calibrated. These errors are reduced after calibration of the SAR data using the DEM. The forest biomass of the north-facing slopes is higher and in better agreement with ground estimates. We have also estimated the dependence of radar backscatter with the incidence angle using multiple incidence angle topography-corrected data, and we have retrieved forest biomass as a function of incidence angle. Surface truth indicates that the results are now comparable in precision to those obtained in the floodplains.

ACKNOWLEDGMENTS

This study was supported by the Swiss Academy of Science and the Holderbank Foundation. A portion of the research described in this paper was performed by the Jet Propulsion Laboratory, California Institute of Technology, under a contract with the National Aeronautics and Space Administration. The authors wish to thank Mr. Timothy Miller (JPL) and Dr. Scott Hensley (JPL) for the several explanations of the navigation systems, Mr. Richard Carande (JPL) for the discussions concerning the processing of the SAR data, and Dr. Jakob van Zyl (JPL) for reviewing the paper.

REFERENCES

DC-8 Airborne Laboratory Experimenters Handbook, Ames Research Center Publisher, Moffett Field, California, 1990.

Holecz F., E. Meier, and D. Nüesch, "Postprocessing of relief induced radiometric distorted spaceborne SAR imagery", Chapter 14 in SAR-Geocoding - Data and Systems, Wichmann-Verlag, edited by Schreier, 1993.

Holecz F., E. Meier, J. Piesbergen, D. Nüesch, and J. Moreira, "Rigorous derivation of the backscattering coefficient", IEEE Geoscience and Remote Sensing Newsletter, No. 92, September, 1994.

Meier E., U. Frei, and D. Nüesch, "Precise terrain corrected geocoded images", Chapter 7 in SAR-Geocoding - Data and Systems, Wichmann-Verlag, edited by Schreier, 1993.

Rignot E., J.B. Way, C. Williams, and L. Viereck, "Radar estimates of aboveground biomass in boreal forest of interior Alaska", IEEE Transactions on Geoscience and Remote Sensing, Vol. 32, No. 5, 1994.

van Zyl J., B. Chapman, P. Dubois, and J. Shi, "The effect of topography on SAR calibration", IEEE Transactions on Geoscience and Remote Sensing, Vol. 31, No. 5, 1993.

REMOTELY SENSED INDICATORS OF HABITAT HETEROGENEITY AND BIOLOGICAL DIVERSITY: A PRELIMINARY REPORT

Marc Imhoff [1], Thomas Sisk [2], Anthony Milne [3], Garth Morgan, and Tony Orr [4]
[1]NASA Goddard Space Flight Center, [2] National Biological Survey, Department of the Interior
[3] University of New South Wales, Australia, [4] DSTO, Australia

INTRODUCTION

The relationship between habitat area, spatial dynamics of the landscape, and species diversity is an important theme in population and conservation biology. Of particular interest is how populations of various species are affected by increasing habitat edges due to fragmentation. Over the last decade, assumptions regarding the effects of habitat edges on biodiversity have fluctuated wildly, from the belief that they have a positive effect to the belief that they have a clearly negative effect. This change in viewpoint has been brought about by an increasing recognition of the importance of geographic scale and a reinterpretation of natural history observations. In this preliminary report from an ongoing project, we explore the use of remote sensing technology and geographic information systems to further our understanding of how species diversity and population density are affected by habitat heterogeneity and landscape composition. A primary feature of this study is the investigation of SAR for making more rigorous investigations of habitat structure by exploiting the interaction between radar backscatter and vegetation structure and biomass (Dobson et al. 1992). A major emphasis will be on the use of SAR data to define relative structural types based on measures of structural consolidation using the vegetation surface area to volume ratio (SA/V). Past research has shown that SAR may be sensitive to this form of structural expression (Imhoff 1994) which may affect biodiversity.

SITE DESCRIPTION AND METHODS

In September, 1993, P-, L-, and C-band SAR data were collected over a section of the South Alligator River in Kakadu National Park in the Australian Northern Territory (NT) as part of the Joint NASA/Australia AIRSAR Deployment. The SAR data were supplemented by Landsat TM imagery captured several days later. The area is tropical and is characterized by estuarine flood plains and freshwater billabongs with paleosol (laterite) uplands and scattered sandstone ridges and outcrops. Elevation differences between the flood plains and the uplands are on the order of only a few meters. There are 16 monsoon rain forest floristic groups, in patches on the uplands and low lying soils containing approximately 33 species of overstory trees of Austral-asian origin. The area has a hot-wet hot-dry climate and 85-95% of the 1400 mm in mean annual precipitation occurs between December and March. In August-September, 1994, field data consisting of vegetation structure and other habitat spatial information and census data on the distribution and density of all bird species within the test site were collected along transects orthogonal to a series of habitat edge gradients in the test area. The research described in this report focuses on a set of two primary habitat edges based on vegetation differences. The edges run roughly east-west in orientation spanning approximately 5 deg in SAR range (52 - 57 deg incidence angle). The gradient changes in a north-south direction which is the azimuth direction of the radar. The area was selected because, while the edges are distinct, one edge is predominantly structural in nature while the other is floristic in nature. The structural edge will be identified henceforth as edge A and the floristic one as edge B.

Birds: Ten north-south trending transects were established at random locations orthogonal to the edge lines, with a minimum separation of 100m and a maximum separation of 200m. Along each transect, census points were placed systematically at intervals of 100m. The southernmost census point was established 200m south of the edge between a wet *Melaleuca* forest and a dry *Melaleuca* woodland (edge A). Each of the ten transects spanned edge A and a second edge (edge B) between the dry *Melaleuca* woodland and open mixed *Eucalypt* woodland. Each transect was censused twice (between 1/2 hr and 3 hrs after sunrise) over ten consecutive days; once beginning at the northern end of the transect, and once beginning at the southern end. Transects were selected arbitrarily each morning, and specific pairings of transects were not repeated. At each census point, 5 minute stationary census were conducted. All birds

seen or heard were recorded, along with an estimate of their distance from the census point, up to a maximum of 50m. Birds detected at distances greater than 50m were not recorded (Reynolds et al. 1980). For each species, abundance, represented by the number of detections per point count, was plotted against the position of the point along the habitat gradient. Frequency of detection was tested against a uniform distribution (G-test) to identify significant changes in abundance at the two edges. In all cases, a probability of $p<.05$ that the observed changes in abundance were due to chance alone was deemed sufficient to reject the null hypothesis that the detections were distributed randomly along the gradient.

Vegetation: Vegetation data were collected along seven of the bird survey lines using the point-center-quarter (PCQ) method. Point data were taken at 33 m intervals and included: species identification, stem diameter (dbh), height, height to live crown, crown dimensions in x and y, and stem density. In all, more than 200 points on the ground were surveyed compiling measurements for over 1000 individual trees. Measurements for crown components such as branch length, number of branches, and leaf area are being made using photographic methods including hemispherical canopy photography. The PCQ data were divided into nine 100 meter wide geographic zones parallel to edges A and B for statistical analysis. Each zone contains a minimum of 21 PCQ points from which statistics were generated. Results are given for floristic composition and vegetation structure including: mean stem density, dbh, height, biomass, and vegetation surface area to volume ratio SA/V.

SAR Analysis: The SAR analysis is in the correlative phase. The Macsigma0 program written by JPL was used to derive backscatter statistics for the 9 vegetation edge zones. Radar backscatter is reported as σ° in dB (m^2/m^2) and is compared to the vegetation (bole) surface area to bole volume ratio (SA/V) and bole biomass.

RESULTS AND DISCUSSION

SAR and Vegetation Structure: The SAR data used in this study successfully identified a series of edaphic driven structural changes across a floristically homogeneous stand of vegetation. Such a change was evident at edge A where a *Melaleuca cajuputi* woodland changed in structure from a tall, closed canopy (zones 1-3) to a more densely stocked formation of smaller individuals (zones 4-6). All of the structural parameters except stem density changed significantly across edge A ($p<.01$, T-test). The SAR data also detected another structural/floristic edge at zone 5 where the *M. cajuputi* changes to a more dense smaller statured stand containing a mixture of *M. cajuputi* and *M. viridiflora*. The bole SA/V changed dramatically in zone 5. All three SAR bands were capable of clearly identifying these changes, yet these changes *were not* as readily discernible on the Landsat TM image. Because the stands in zones 1-6 are nearly monospecific, substantial changes in the canopy opening were required before the ground contribution could alter the otherwise identical TM spectral reflectance from the canopy. Edge B represents the opposite situation from edge A. At edge B there is an abrupt and complete floristic change but the structural differences are more subtle. Only crown volume was significantly different ($p< .01$, T-test). In the case of edge B, bole biomass does change significantly but this is due to the higher bulk density of *Eucalypts* and not to a bole volume difference. The best correlations were achieved between the C-HV, L-VV, P-VV and C-VV, L-VV, P-VV backscatter and bole biomass and SA/V respectively (Figure 1).

Birds and Vegetation Structure: During the census, 1449 positive identifications were made representing 58 species. Here we represent data for three avian species that illustrate the range of responses observed across the habitat gradient. The lemon-bellied flycatcher (*Microeca flavigaster*) responded primarily to floristics (Figure 2a). It was associated with habitats dominated by both *Melaleuca* species, and abundance did not change significantly at the structural edge (edge A). At edge B where vegetation structure did not change dramatically, but where *Melaleuca*-dominated woodland was replaced by mixed *Eucalypt* woodland, the species declined significantly. The brown honeyeater (*Lichmera indistincta*) followed a different pattern. It occurred abundantly throughout the study site (Figure 2b) and its density did not change markedly in the different vegetation communities. Its significant increase at edge B and a smaller increase at zone 5, indicates that this species may be responding to some structural aspects of its habitat. Some significant structural shifts did occur at zone 5 (SA/V) and edge B (crown volume). The yellow oriole (*Oriolus flavocintus*) seems to be strongly associated with wet *Melaleuca* forests (Figure 2c). Within this habitat it occurred with greater frequency at the edge. This species appears to be responding strongly to both floristic and structural elements, generating a more complex edge-associated response.

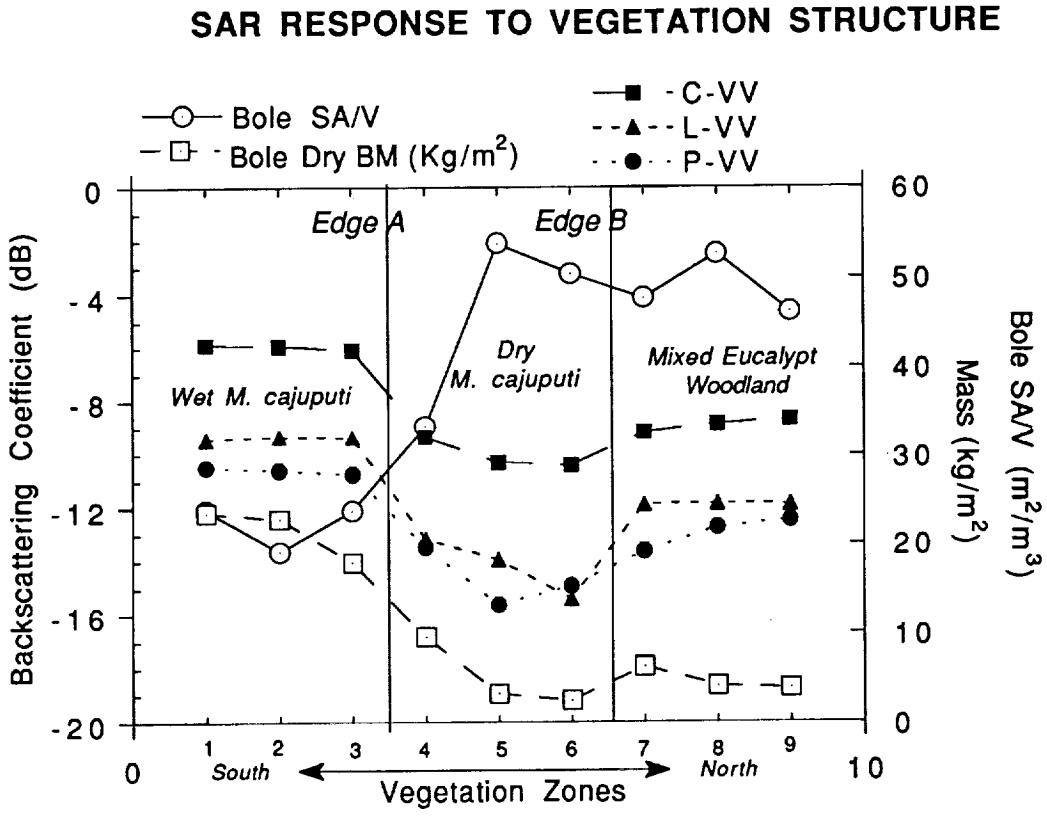

Figure 1. SAR response to vegetation structure and biomass along the habitat gradient. As biomass decreases across the gradient SA/V increases and SAR backscatter decreases. All changes in structural parameters except stem density were significant across edge A, as was SA/V at zone 5 ($p<.01$, T-test). Few structural changes were statistically significant across edge B. Bole volume differences across edge B are not significant, but biomass changes are more evident due to bulk density differences between the *Melaleuca* and the *Eucalypts*.

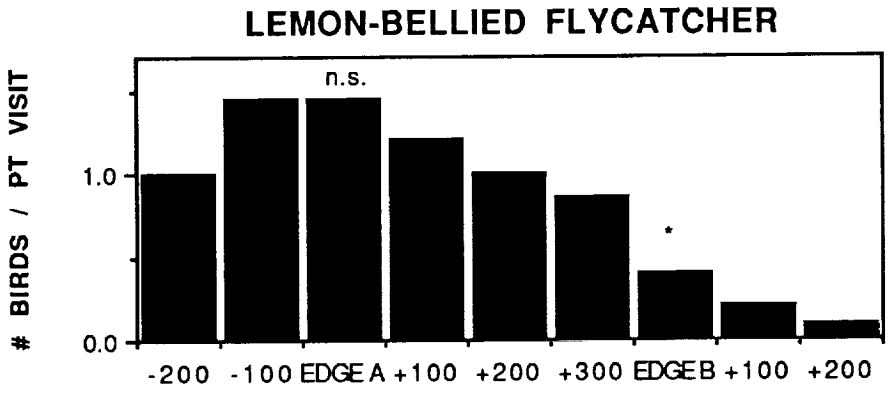

Figure 2a. Abundance response to vegetation for the lemon-bellied flycatcher (*Microeca flavigaster*) which responded primarily to floristics. Change is significant (* = $p \leq .05$) at edge B but not at edge A (n.s.). Histogram blocks correspond to vegetion zones 1-9 as shown in Figure 1.

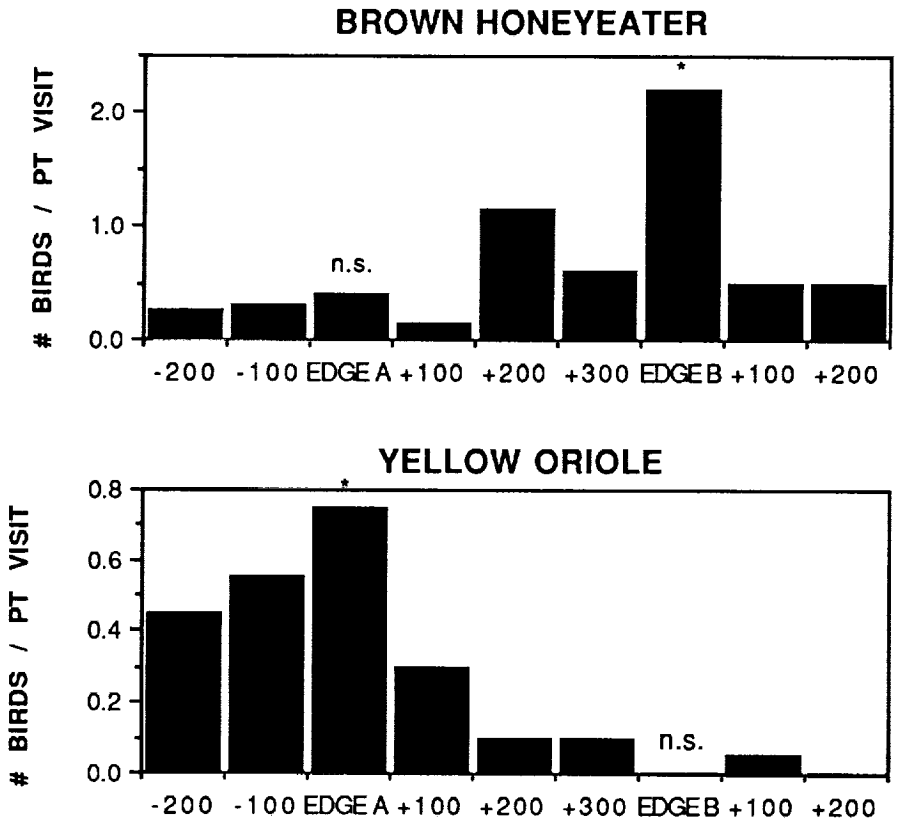

Figures 2b and 2c. Top: Abundance response to vegetation for the brown honeyeater (*Lichmera indistincta*). Abundances for this species did not change markedly in the different vegetation communities. Change is significant at edge B (* = p≤ .05) but not edge A (n.s.). Bottom : Abundance response for the yellow oriole (*Oriolus flavocintus*) is strongly associated with wet *Melaleuca* forests. Change is significant (* = p≤ .05) for edge A but not edge B (n.s.). Histogram blocks correspond to vegetion zones 1-9 as shown in Figure 1.

CONCLUSION

Results from this study indicate that bird species are individualistic in their responses to habitat heterogeneity and that edges are potentially powerful factors in determining the abundance of bird species in a heterogeneous landscape. Through the integration of SAR and TM data with field data we were able to isolate trends in floristic and structural components of bird habitats. We found that different bird species responded differently to these structural factors and that SAR data are capable of identifying some of those structural factors. The combination of SAR, multispectral, and species-level ecological data may provide the foundation for a new generation of modeling tools designed to make predictions of relative species abundances in heterogeneous landscapes based on spatial patterns in the distribution of habitat types.

REFERENCES

Dobson, M. C., E. P. Wilcox, and F. T. Ulaby, 1993, "Effects of Forest Structure on Radar Response to Biomass", *1993 IEEE .Geosci. Remote Sensing, Symposium Tokyo, Japan* vol. 2 page 383

Imhoff, M. L. 1994, "A Theoretical Analysis of the Effect of Forest Structure on SAR Backscatter: Ramifications for Biomass Inventory", *IEEE Trans. Geosci. Remote Sensing*, In Press.

Reynolds, R.T., J.M. Scott, and R.A. Nussbaum 1980, "A Variable Circular Plot Method for Estimating Bird Numbers", *Condor* 82:309-313.

POLARIZATION AND WAVELENGTH DIVERSITIES OF GULF STREAM FRONTS IMAGED BY AIRSAR

J.S. Lee, R.W. Jansen, G.O. Marmorino, S.R. Chubb

Remote Sensing Division, Code 7260
Naval Research Laboratory
Washington DC 20375-5351

1. INTRODUCTION

During the 1990 Gulf Stream Experiment, NASA/JPL AIRSAR imaged the north edge of the Gulf Stream near the coast of Virginia (see Fig.1). Simultaneous in-situ measurements of currents, temperatures, salinities, etc. were made for several crossings of the north edge by the R/V Cape Henlopen (Marmorino et al., 1994).

Measurements identified two fronts with shearing and converging flows. The polarimetric SAR images from the fronts showed two bright linear features. One of them corresponds to the temperature front, which separated the warm Gulf Stream water to the south from a cool, fresh-water filament to the north. The other line, located about 8 km north of the temperature front, is believed to correspond to the velocity front between the filament and the slope water. At these fronts, wave-current interactions produced narrow bands of steep and breaking waves manifesting higher radar returns in polarimetric SAR images. A schematic diagram summarizing the observations is shown in Fig. 2.

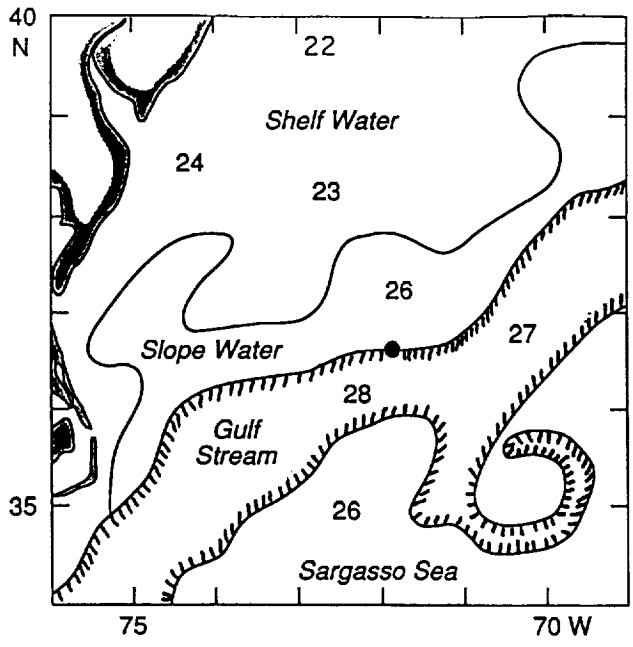

Fig. 1 The 1990 Gulf Stream Experiment site is shown as a black dot. Ocean surface temperature (in degree Celsius) reveals that Gulf Stream and slope water temperatures differ by two degrees.

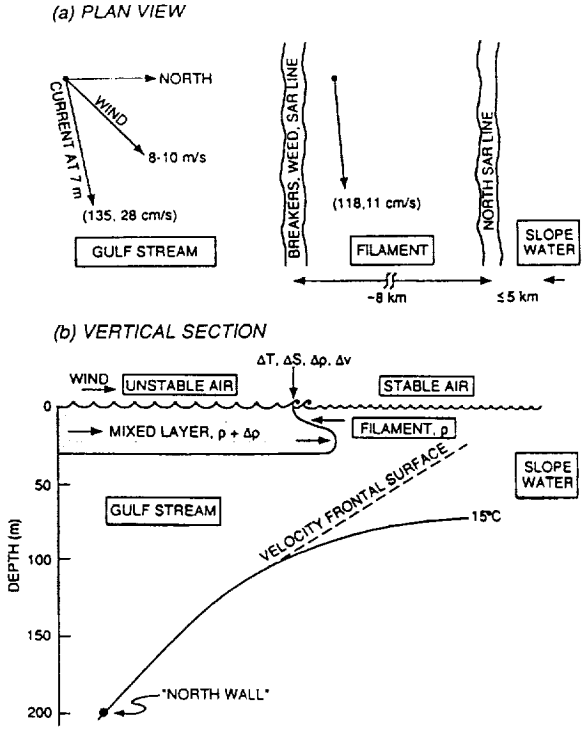

Fig. 2. Schematic diagram of the observations. (a) Plan view shows the temperature front on the left and the velocity front on the right. (b) Vertical section view indicates relative cross-front current motion and surface convergence.

In general, our AIRSAR imagery shows that the signal-to-clutter ratio of radar cross sections for the temperature front is higher than that of the velocity front. In this paper, we study the polarization and wavelength diversities of radar response of these two fronts using the P-, L- and C-Band Polarimetric SAR data. The north-south flight path of the AIRSAR crossed the temperature front several times and provided valuable data for analysis. Three individual passes are investigated. We found that for the temperature front, the cross-pol (HV) responses are much higher than co-pol responses (VV and HH), and that P-Band HV has the highest signal to clutter ratio. For the velocity front, the ratio is the strongest in P-Band VV, and it is indistinguishable for all polarizations in C-Band.

The radar cross sections for all three polarization (HH, HV and VV) and for all three bands are modelled using an ocean wave model (Jansen et al., 1993) and a composite Bragg scattering model. In our initial investigations, the theoretical model agrees qualitatively with the AIRSAR observations.

2. AIRSAR OBSERVATIONS

SAR images from several AIRSAR passes across the north boundary of the Gulf Stream have been analyzed. Due to the page limitation, images from one pass only are shown in Fig. 3. The altitude of the JPL/DC-8 was 5.5 km, and it was traveling from north to south. The resolution is 12.1 m in azimuth and 6.7 m in slant range. Each image is 12.4 km in north-south extent and near 9 km in slant range. The near range is on the left, and the range of incidence angles across the images is 25 to 60 degrees. Images are oriented with north toward the top. The R/V Cape Henlopen was traveling north, and is shown with its wake in the upper left part of each image.

The P-Band HV image (Fig. 3A) clearly shows the temperature front as a bright line located at the lower part of the image, and the velocity front is shown at 8 km toward north with a wide dark strip before it. The response of the temperature front is much weaker for P-Band VV as shown in Fig. 3B, but the velocity front is more distinct. The C-Band images (Fig. 3C and 3D) exhibit distinctive wavelength diversity in radar response. The velocity front is almost invisible, and the signal to clutter ratios of the temperature front are detectable but weaker than that of P-Band. The V shaped dark region in Fig. 3D was due to the wave damping attenuation by rain. Wave damping is most pronounced for waves shorter than 25 cm (L-Band) (Tsimplis, 1992). However, this effect is almost absent in the cross-polarization image (C-Band HV, Fig. 3C).

Several other north-east SAR passes have also been analyzed. Similar SAR responses in polarization and wavelength were observed. In general, the temperature front is more visible than the velocity front. For the temperature front, the HV polarization has much higher signatures than co-polarizations, and P-band HV has the highest signal to clutter ratio, followed by L-Band and C-Band. From in situ measurements and observations by video camera, surface current convergence was evident by the narrow width of the temperature front, an adjacent band of breaking waves, and the accumulation of Sargassum. The presence of strong signature in HV polarization indicates significant wave-current interaction from large surface tilts and possibly breaking waves, which causes higher order scattering. It is interesting to note that P-Band VV polarization has a very weak signature for the temperature front. For the velocity front, the P-Band is much weaker, and has the strongest signature among the three bands. The velocity front is invisible in the C-band images. In all three bands, the VV polarization has the strongest signature followed by HV and HH.

3. VERIFICATION WITH OCEAN WAVE MODEL

Theoretical predictions were made for the temperature front where in-situ data was available. The modelling for the velocity front will not be addressed here for lack of measurements. The temperature front is predominantly a current convergence which was modelled

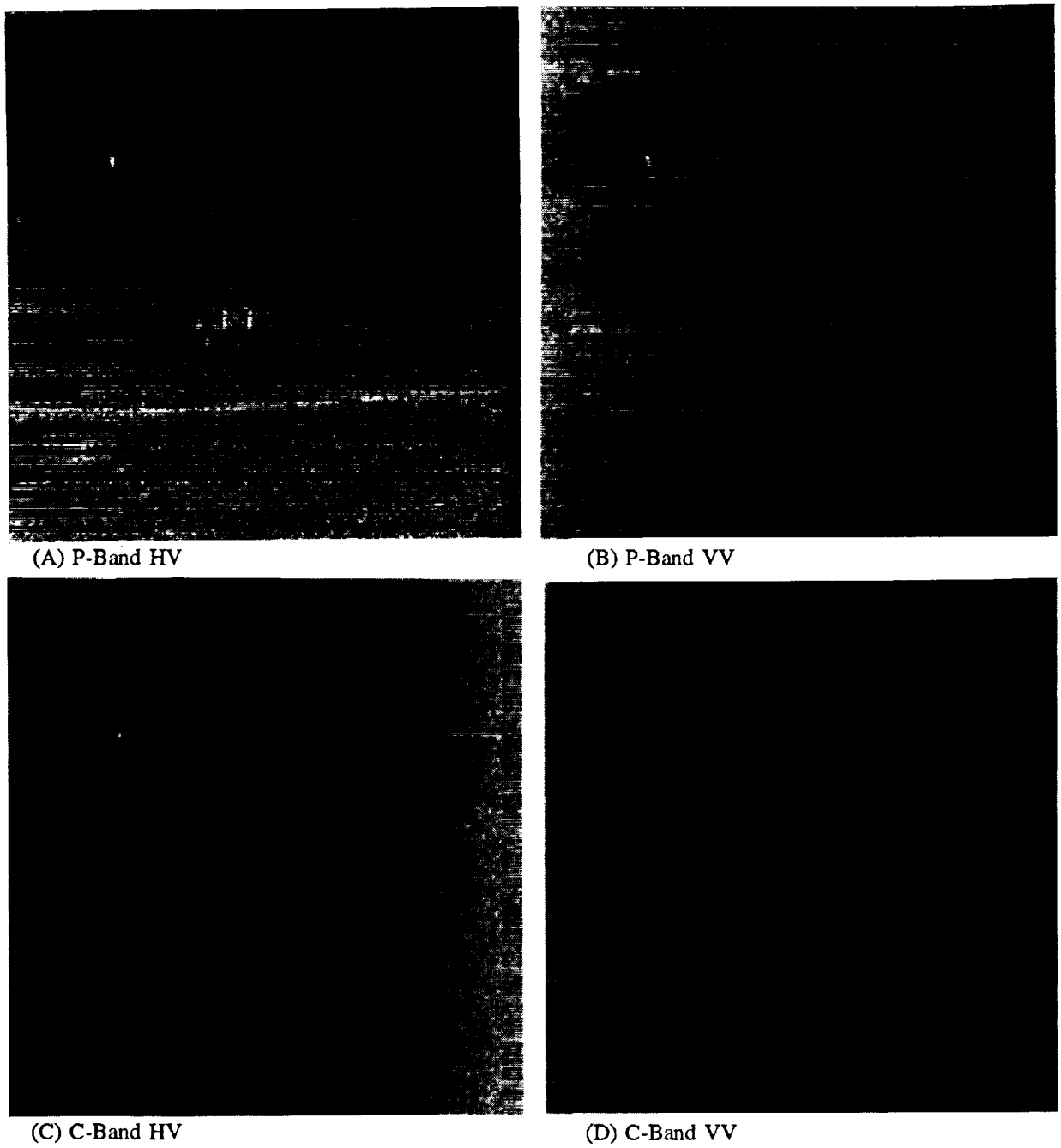

(A) P-Band HV

(B) P-Band VV

(C) C-Band HV

(D) C-Band VV

Fig. 3 P-Band and C-Band Polarimetric SAR imagery of Gulf Stream fronts. North is toward the top. The AIRSAR was flying from north to south. The R/V Cape Henlopen was traveling northbound, and is shown with its wake in the upper left part of each image. (A) The P-Band HV image clearly shows the temperature front in the lower part of the image, and it also shows a dark wide strip before the velocity front, which is located 8 km to the north of the temperature front. (B) The P-Band VV image, however, has much a smaller radar response at the temperature front, but the velocity is more distinct. (C) The C-Band HV image shows the temperature front less well-defined than the P-Band. (D) The C-Band VV shows the damping attenuation by rain and other effects on the response of the temperature front. The cross sections of the velocity front in both C-Band images are very weak, making the fronts nearly indistinguishable.

as the one-dimensional function,

$$V(y) = -\frac{\delta V}{2} \tanh\left(\frac{y}{\delta y/2}\right)$$

The depth and current widths were taken to be δy=100m and δV=25cm/s, consistent with shipboard estimates. This current was used as an input into the action density equation with a Plant-Hughes type source to derive the ocean wave spectrum near the temperature front (see Jansen et al, 1993). The radar image modulation is then predicted using the wave field slope statistics in a composite scattering radar model. We do not consider the effects of velocity bunching or speckle, which would be present in a more complete SAR model.

Fig. 4A shows the P-Band HH, HV and VV radar modulation around the temperature front at 45 degree incidence angle, using the ocean wave model but excluding any contribution from breaking waves. The HV polarization has a much higher radar modulation than both the HH and the VV. This agrees with our observations on polarization diversity for the temperature front. Fig. 4B shows the cross-section dependence on wavelength. For the cross-polarization (HV), P-Band has the highest value with peak near 2.0 dB, and L-Band and C-Band are 1.6 and 1.1, respectively. This theoretical result also verifies our observed trend in wavelength diversity.

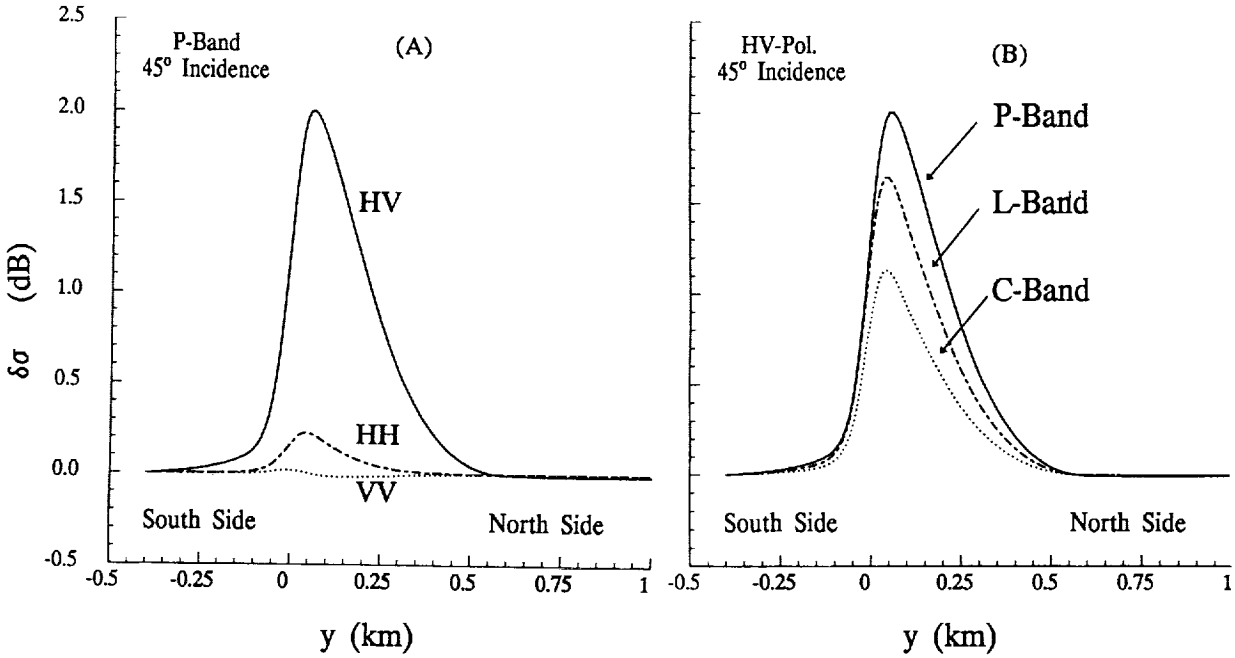

Fig. 4 Theoretical modeling of radar modulations of the temperature front at 45 degree incidence. This model does not include the breaking waves. The horizontal axis indicates the distance in km from the temperature front. (A) The P-Band HV cross-section values are much higher than the comparable of HH and VV. (B) Peak-values for HV polarization for P-, L- and C-Band, respectively are 2.0, 1.6 and 1.1. These results qualitatively confirms the AIRSAR measurements.

REFERENCES

[1] Jansen,R.W. et al, 1993, "Modeling of Gulf Stream Boundary Features in SAR Imagery," IGARSSS'93 Proceedings, 550-552.

[2] Marmorino, G.O. et al, 1994, "Gulf Stream Surface Convergence Imaged by Synthetic Aperture Radar," JGR, 99(C9), 18,315-18,328.

[3] Tsimplis, M.N., 1992, "The effect of rain in calming the sea," J. Phys. Oceanogr., 22, 404-412.

Bayes Classification of Interferometric TOPSAR Data

T.R. Michel, E. Rodriguez, B. Houshmand, R. Carande

Jet Propulsion Laboratory

California Institute of Technology

Pasadena, California 91109

(818)354-0918; trm@sibyl.jpl.nasa.gov

We report the Bayes classification of terrain types at different sites using airborne interferometric synthetic aperture radar (INSAR) data. A Gaussian maximum likelihood classifier was applied on multidimensional observations derived from the SAR intensity, the terrain elevation model, and the magnitude of the interferometric correlation. Training sets for forested, urban, agricultural, or bare areas were obtained either by selecting samples with known ground truth, or by k-means clustering of random sets of samples uniformly distributed across all sites, and subsequent assignments of these clusters using ground truth. The accuracy of the classifier was used to optimize the discriminating efficiency of the set of features that was chosen. The most important features include the SAR intensity, a canopy penetration depth model, and the terrain slope.

We demonstrate the classifier's performance across sites using a unique set of training classes for the four main terrain categories. The scenes examined include San Francisco (predominantly urban and water), Mount Adams (WA) (forested with clear cuts), Pasadena (urban with mountains), and Antioch Hills (CA) (water, swamps, fields). Issues related to the effects of image calibration and the robustness of the classification to calibration errors are explored. The relative performance of single polarization Interferometric data classification is contrasted against classification schemes based on polarimetric SAR data.

ACKNOWLEDGMENT

The research described in this paper was performed by the Jet Propulsion Laboratory, California Institute of Technology, under a contract with the National Aeronautics and Space Administration and with the Advanced Research Projects Agency (ARPA).

TERRAIN CLASSIFICATION USING CIRCULAR POLARIMETRIC FEATURES

David G. Michelson and Ian G. Cumming
University of British Columbia, Vancouver, B.C., Canada V6T 1Z4
E-mail: davem@ee.ubc.ca and ianc@ee.ubc.ca

Charles E. Livingstone
Canada Centre for Remote Sensing, Ottawa, Ont., Canada K1A 0Y7
E-mail: livingstone@ccrs.emr.ca

1 Introduction

Conventional representations of polarization response are referred to a horizontally and vertically polarized basis. Recent studies by Freeman and Durden [1], van Zyl [2], and others suggest that alternative polarimetric features which more easily resolve the contributions of simple scattering mechanisms such as odd-bounce, even-bounce, and diffuse scattering could offer several advantages in terrain classification. The circular polarization covariance matrix is a potential source of such features. In this paper, we derive its relationship to the Stokes matrix, describe some of its properties, and compare the utility of linear and circular polarimetric features in classifying an AIRSAR scene containing urban, park, and ocean terrain.

2 Properties of the Circular Polarization Covariance Matrix

In the monostatic case, the circular polarization covariance matrix $[C]$ is given in terms of the elements of the circular polarization scattering matrix, S_{ll}, S_{lr}, S_{rl}, and S_{rr}, by the reduced form

$$[C] = \begin{bmatrix} \langle S_{ll}S_{ll}^* \rangle & \langle S_{ll}S_{lr}^* \rangle & \langle S_{ll}S_{rr}^* \rangle \\ \langle S_{lr}S_{ll}^* \rangle & \langle S_{lr}S_{lr}^* \rangle & \langle S_{lr}S_{rr}^* \rangle \\ \langle S_{rr}S_{ll}^* \rangle & \langle S_{rr}S_{lr}^* \rangle & \langle S_{rr}S_{rr}^* \rangle \end{bmatrix}, \tag{1}$$

where, by definition, $S_{lr} = S_{rl}$. In this format, the polarization responses of odd-bounce, even-bounce, and diffuse scatterers are given by

$$[C_o] = \begin{bmatrix} 0 & 0 & 0 \\ 0 & 1 & 0 \\ 0 & 0 & 0 \end{bmatrix}, \quad [C_o] = \begin{bmatrix} 1 & 0 & 1 \\ 0 & 0 & 0 \\ 1 & 0 & 1 \end{bmatrix}, \quad [C_d] = \begin{bmatrix} 1 & 0 & 0 \\ 0 & 1 & 0 \\ 0 & 0 & 1 \end{bmatrix}, \tag{2}$$

respectively. It can be shown that the representation of the target response after rotation of the target by an angle α is given by

$$[C'] = \begin{bmatrix} S_{ll}S_{ll}^* & S_{ll}S_{lr}^* e^{-j2\alpha} & S_{ll}S_{rr}^* e^{-j4\alpha} \\ S_{lr}S_{ll}^* e^{j2\alpha} & S_{lr}S_{lr}^* & S_{lr}S_{rr}^* e^{-j2\alpha} \\ S_{rr}S_{ll}^* e^{j4\alpha} & S_{rr}S_{lr}^* e^{j2\alpha} & S_{rr}S_{rr}^* \end{bmatrix} \tag{3}$$

The diagonal elements and the magnitude of the off-diagonal elements are both invariant under rotation of either the target or the radar antenna about the line-of-sight.

In order to derive an expression for the elements of the circular polarization covariance matrix in terms of the elements of the Stokes matrix, it is necessary to express the Stokes vector **J** with respect to a circularly polarized basis. Thus,

$$\mathbf{J} = \begin{bmatrix} E_\ell E_\ell^* + E_r E_r^* \\ E_\ell E_r^* + E_r E_\ell^* \\ j(E_\ell E_r^* - E_r E_\ell^*) \\ E_\ell E_\ell^* - E_r E_r^* \end{bmatrix} = \begin{bmatrix} |E_\ell|^2 + |E_r|^2 \\ 2\Re(E_\ell\, E_r^*) \\ 2\Im(E_\ell\, E_r^*) \\ |E_\ell|^2 - |E_r|^2 \end{bmatrix} = \begin{bmatrix} a_\ell^2 + a_r^2 \\ 2a_\ell a_r \cos\delta_c \\ 2a_\ell a_r \sin\delta_c \\ a_\ell^2 - a_r^2 \end{bmatrix} . \quad (4)$$

where $E_\ell = a_\ell e^{j\delta_\ell}$ and $E_r = a_r e^{j\delta_r}$ are the complex amplitudes of the left and right circularly polarized components of the electric field, respectively, and $\delta_c = \delta_r - \delta_l$ is the circular polarimetric phase difference. A derivation similar to that employed by van Zyl and Ulaby [3] for the linearly polarized case yields expressions for the elements of the circular polarization covariance matrix in terms of the elements of the Stokes matrix:

$$\begin{aligned} S_{\ell\ell}S_{\ell\ell}^* &= a_{11} + 2a_{14} + a_{44} , \\ S_{rr}S_{rr}^* &= a_{11} - 2a_{14} + a_{44} , \\ S_{\ell r}S_{\ell r}^* &= a_{11} - a_{44} , \\ S_{\ell\ell}S_{rr}^* &= (a_{22} - a_{33}) - j2a_{23} , \\ S_{\ell r}S_{rr}^* &= (a_{12} - a_{24}) - j(a_{13} - a_{34}) , \\ S_{\ell\ell}S_{\ell r}^* &= (a_{12} + a_{24}) - j(a_{13} + a_{34}) . \end{aligned} \quad (5)$$

For scattering by azimuthally isotropic terrain, symmetry dictates that the ensemble average of the cross-products of the co-polarized (HH and VV) and the cross-polarized (HV) elements of the linear polarization scattering matrix will be zero, as noted by Borgeaud *et al.* [4] and van Zyl [5]. In this case, the corresponding linear polarization covariance matrix has dimensionality of five. It can be shown that the equivalent circular polarization covariance matrix is given by

$$[C] = \begin{bmatrix} S_{\ell\ell}S_{\ell\ell}^* & S_{\ell\ell}S_{\ell r}^* & S_{\ell\ell}S_{rr}^* \\ S_{\ell r}S_{\ell\ell}^* & S_{\ell r}S_{\ell r}^* & S_{\ell r}S_{rr}^* \\ S_{\ell\ell}S_{rr}^* & S_{\ell\ell}S_{\ell r}^* & S_{\ell\ell}S_{rr}^* \end{bmatrix} = \begin{bmatrix} A & C - jD & A \\ C + jD & B & C + jD \\ A & C - jD & A \end{bmatrix} , \quad (6)$$

where

$$\begin{aligned} A &= a_{11} + a_{44} , \\ B &= a_{11} - a_{44} , \\ C &= a_{12} , \\ D &= a_{34} . \end{aligned}$$

The quantitites A, B, and $|C \pm jD|$ are rotation-invariant. The cross-product $S_{\ell\ell}S_{rr}^*$, which is generally a complex quantity, is real in this case. Note that the circular polarization covariance matrix representation of an azimuthally isotropic scatterer has a dimensionality of four.

3 Experimental Results

A comparison of the utility of linear and circular polarimetric features in classifying ground cover and terrain was performed using the May 15, 1985 L-band AIRSAR image of San Francisco. The near range portion of the image in which the look angle was less than 30 degrees was excluded. Training areas for urban, park, and ocean classes were defined as shown in Figure 1(a). A minimum distance decision rule was used to classify each pixel in the image. The averaging box size for computing the Stokes matrix was 2 × 2. In the linearly polarized case, the features used were the total power, $\langle S_{hh}S_{hh}^* \rangle$, $\langle S_{vv}S_{vv}^* \rangle$, $\langle S_{hv}S_{hv}^* \rangle$, $\Re\langle S_{hh}S_{vv}^* \rangle$ and $\Im\langle S_{hh}S_{vv}^* \rangle$. In the

circularly polarized case, the features used in classification were the total power, $\langle S_{ll} S_{ll}^* \rangle$, and $\langle S_{lr} S_{lr}^* \rangle$.

The results of classification are presented in Figure 1 and are summarized in Tables 1 and 2. Although both classifiers were able to distinguish ocean from urban and park with ease, the choice between urban and park was slightly less certain. The linear polarimetric classifier tended to classify more pixels as urban than the circular polarimetric classifier, particularly in the area to the north-west of the Golden Gate Bridge and the western shoreline of the city. Confusion matrices for self-classification of training areas are presented in Table 2. They suggest that the circular polarimetric classifier was more consistent in classifying urban areas than the linear polarimetric classifier and may therefore have provided slightly better classification accuracy.

Table 1: Confusion Matrix for Classification of an AIRSAR Image of San Francisco

		Linear Polarimetric Classifier			
	Class	Unclas.	Urban	Park	Ocean
Circular Polarimetric Classifier	Unclas.	4.3%	0.6%	0.2%	0.0%
	Urban	0.3%	22.9%	6.0%	0.0%
	Park	0.1%	3.5%	24.2%	0.7%
	Ocean	0.4%	0.0%	2.2%	34.6%

Table 2: Confusion Matrices for Self-Classification of Training Areas

Linear Polarimetric Classifier

	Training Area		
Class	Urban	Park	Ocean
Unclas.	6.6%	0.1%	0.0%
Urban	63.8%	9.8%	0.0%
Park	29.4%	89.4%	0.0%
Ocean	0.3%	0.8%	100.0%

Circular Polarimetric Classifier

	Training Area		
Class	Urban	Park	Ocean
Unclas.	6.7%	0.7%	0.0%
Urban	70.5%	9.9%	0.0%
Park	22.2%	87.6%	0.0%
Ocean	0.7%	1.8%	100.0%

4 Conclusions

We have defined the circular polarization covariance matrix, derived its relationship to the Stokes matrix, and described some of its properties. These properties include the invariance of the magnitude of its elements with respect to rotation of the sensor or the scatterer about the radar line-of-sight and the form of the response of an azimuthally isotropic scatterer. The results of classifying urban, park, and ocean terrain in an AIRSAR scene of San Francisco using linear and circular polarimetric features have been presented and compared. The next step will be to compare the utility of features derived from the linear and circular polarization covariance matrices in classifying representative scenes of sea ice, boreal forest, and agricultural fields.

References

[1] A. Freeman and S. Durden, "A three-component scattering model to describe polarimetric SAR data," in *Radar Polarimetry* (H. Mott and W.-M. Boerner, eds.), Proc. SPIE, vol. 1748, pp. 213–224, 1993.

[2] J. J. van Zyl, "Application of Cloude's target decomposition theorem to polarimetric imaging radar data," in *Radar Polarimetry* (H. Mott and W.-M. Boerner, eds.), Proc. SPIE, vol. 1748, pp. 184–191, 1993.

[3] J.J. van Zyl and F.T. Ulaby, "Scattering matrix representation for simple targets," in *Radar Polarimetry for Geoscience Applications*, F. T. Ulaby and C. Elachi, eds., Norwood, MA: Artech House, 1990, pp. 17–52.

[4] M. Borgeaud, R.T. Shin, and J.A. Kong, "Theoretical models for polarimetric radar clutter," *J. Electromag. Waves Applic.*, vol. 1, no. 1, pp. 73–89, 1987.

[5] J. J. van Zyl, "Unsupervised classification of scattering behavior using radar polarimetry data," *IEEE Trans. Geosci. Remote Sensing*, vol. GE-27, pp. 36–45, Jan. 1989.

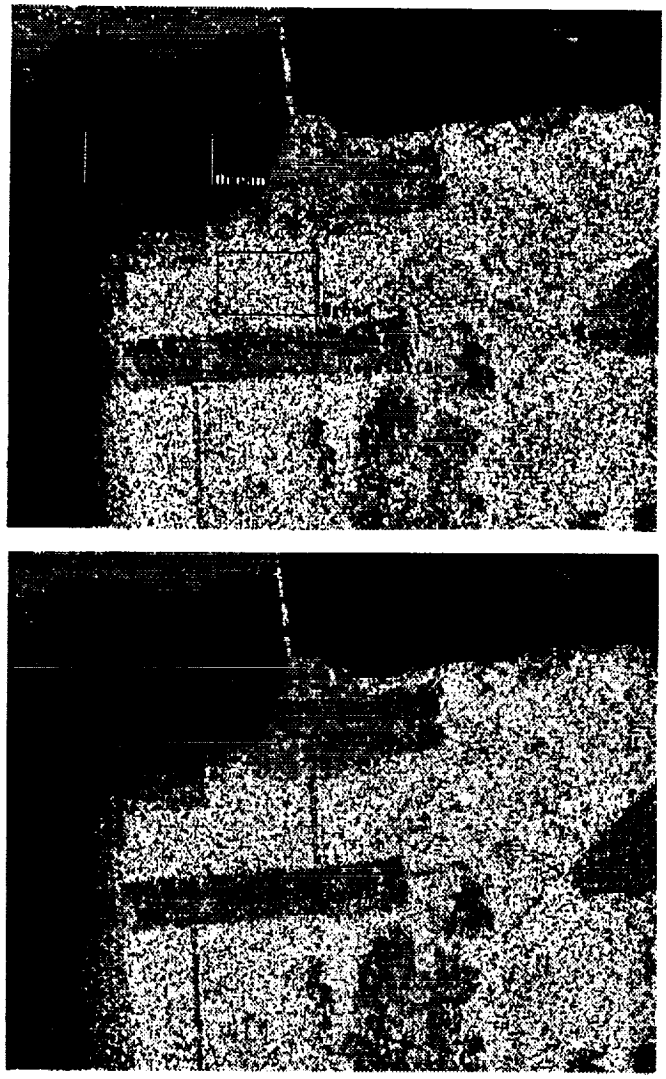

Figure 1: Minimum distance classification of an L-band AIRSAR image of San Francisco using (top) linearly polarized and (bottom) circularly polarized features. Training areas are indicated. Classification legend: urban - white; park - light gray; ocean - black; unclassified - dark gray.

USE OF AIRSAR TO IDENTIFY WOODY SHRUB INVASION AND OTHER INDICATORS OF DESERTIFICATION IN THE JORNADA LTER

H. Brad Musick
University of New Mexico, Albuquerque, New Mexico

Gerald G. Schaber and Carol S. Breed
U. S. Geological Survey, Flagstaff, Arizona

1. INTRODUCTION

The replacement of semidesert grassland by woody shrubland is a widespread form of desertification. This change in physiognomy and species composition tends to sharply reduce the productivity of the land for grazing by domestic livestock, increase soil erosion and reduce soil fertility, and greatly alter many other aspects of ecosystem structure and functioning (Schlesinger *et al.*, 1990).

Remote sensing methods are needed to assess and monitor shrubland encroachment. Detection of woody shrubs at low density would provide a particularly useful baseline on which to access changes, because an initially low shrub density often tends to increase even after cessation of the disturbance (e.g., overgrazing, drought, or fire suppression) responsible for triggering the initial stages of the invasion (Grover and Musick, 1990). Limited success has been achieved using optical remote sensing. In contrast to other forms of desertification, biomass does not consistently decrease with a shift from grassland to shrubland. Estimation of green vegetation amount (e.g., by NDVI) is thus of limited utility, unless the shrubs and herbaceous plants differ consistently in phenology and the area can be viewed during a season when only one of these is green (Musick, 1984).

The objective of this study was to determine if the potential sensitivity of active microwave remote sensing to vegetation structure could be used to assess the degree of shrub invasion of grassland. Polarimetric Airborne Synthetic Aperture Radar (AIRSAR) data were acquired for a semiarid site containing varied mixtures of shrubs and herbaceous vegetation and compared with ground observations of vegetation type and other land-surface characteristics. In this preliminary report we examine the response of radar backscatter intensity to shrub density. The response of other multipolarization parameters will be examined in future work.

2. METHODS

2.1 Study Site

The study site is located in the southern Jornada del Muerto plain in south-central New Mexico. The area includes the study site of the Jornada Long-Term Ecological Research (LTER) Project. Also included in the area are private and BLM-managed grazing land and two long-established range management research facilities (USDA/ARS Jornada Experimental Range and New Mexico State University College Ranch). The U.S. Geological Survey maintains an instrumented test site for studies of climatic conditions and wind erosion on the Experiment Range.

The terrain covered by the data sets has low relief. A wide variety of soils are represented, with surface soil texture ranging from sandy and loamy on uplands to silty and clayey in swales and depressions. Gravelly soils are also common on alluvial fans at the eastern margin of the plain, but were not sampled in this study.

Grassland occupied >90% of the area in the mid-19th century, but shrubland encroachment has now reduced grassland area to less than 25% (Buffington and Herbel, 1965). Some adjacent pastures differing in grazing history exhibit sharply defined boundaries between shrubland and herbaceous vegetation, and distinct shrub-free patches surrounded by shrubland have been created by herbicide treatment and mechanical removal of shrubs. Mesquite (*Prosopis juliflora*) is the most abundant woody shrub; others include *Acacia* spp., tarbush (*Flourensia cernua*), and creosotebush (*Larrea tridentata*). Another common invader of grasslands is broom snakeweed (*Gutierrezia sarothrae*), a perennial subshrub. This species is woody only at the base of the stems (Pieper and McDaniel, 1989) and is thus not considered a woody shrub.

Multifrequency, fully polarimetric, SAR data were acquired at X-band (3-cm wavelength), L-band (24 cm), and P-band (68 cm) on August 1, 1990, by NASA's Airborne Synthetic Aperture Radar (AIRSAR) platform (DC-8) during the summer growing season. Rainfall during the previous month was greater than normal, and both herbaceous plants and shrubs were in leaf and green. During the week before the overflight, most rain gauges on the Jornada Experimental Range recorded from 6 mm to more than 12 mm of rain, and rain fell over much of the area on the day of the overflight (R. P. Gibbens, pers. comm.). Soil moisture content can thus be assumed to have been relatively high, although spatially variable.

Two of the three parallel flightlines barely overlapped and covered an area approximately 30 km along-track by 22 km across-track. The area covered by the third flightline was centered over the other two lines. Sites covered by the third flightline could thus be viewed at contrasting incidence angles.

2.2 Ground Truth

Field observations were made August 17-27, 1993. Changes in shrub density since the 1990 overflight were assumed to be slight. This assumption is based on 15 years of field experience in the area by the senior author, including repeated quantitative measurement of vegetation. In addition, several sites previously sampled and photographed in 1981-82 (Warren and Hutchinson, 1984) were revisited in 1993 and found to have changed little in shrub density.

Fifty-nine sites were visited in the field and delineated as polygons on black-and-white prints of the imagery. Sites were selected to be relatively homogeneous in vegetation and radar signature. Sites were photographed and visual estimates of vegetation composition and soil properties were recorded.

The sites were classified primarily according to percentage of ground area covered by woody shrub canopies (Table 1).

Table 1. Woody Shrub Cover Classes

Class	Woody Shrub Cover %
1	<1
2	1-5
3	5-25
4	>25

The density and composition of herbaceous vegetation varied widely at the lower shrub densities. Class 1 included sites ranging from bare ground to the densest grassland sites, which were in swales that receive extra moisture from runoff. The major woody shrub species on most sites was mesquite, but some sites were dominated by other shrub species.

An additional class (Class Y) was defined after preliminary analyses indicated that sites with a relatively high density of soaptree yucca (*Yucca elata*) had a distinctive radar signature. Stems of this species are unbranched to sparsely branched, 10-15 cm in diameter, 0.5-3.0 m tall, fibrous and high in water content. A conical to nearly spherical spray of narrow, fibrous leaves is borne at the apex of each stem. Understory vegetation of sites in Class Y varied widely, from grassland to dense shrubs.

2.3 AIRSAR Data Calibration and Processing

The multifrequency and fully polarimetric SAR data used in this study were processed at JPL using SAR processor version 2.40. Four 6-foot high aluminum corner reflectors provided by JPL were deployed with an inclination angle of 10 degrees on a smooth (radar dark) playa surface within the Jornada site. These reflectors were imaged during two of the three flightlines. The reflector responses were analyzed using MacSigma0 calibration software provided by the Jet Propulsion Laboratory (Norikane and Freeman, 1993). Calibration correction factors for radar backscatter and phase angles for all three SAR frequencies were computed using the corner reflector analysis software available as part of MacSigma0.

Radar backscatter intensity values for each of the fifty-nine visited sites mentioned above were computed for each SAR frequency and polarization after applying the correction factors derived using the corner reflectors. Some of the field sites were imaged during more than one of the three AIRSAR passes.

3. RESULTS AND DISCUSSION

We first sought a means of eliminating or minimizing the influence of incidence angle on backscattering power intensity. A preliminary examination indicated that variation in σ^0 (backscattering coefficient) with incidence angle for a given site or for sites of a given class was negligible for cross-polarized backscatter at incidence angles $>48°$. Backscattering coefficients for cross-polarized C, L and P band were examined for the 46 sites meeting this incidence angle criterion.

L-HV (horizontal transmit, vertical receive polarization) data provided the greatest separability of shrub density classes (Fig. 1). Backscattering coefficients increased with shrub cover, and appeared to be especially sensitive at low levels of shrub cover (e.g., in discriminating between Classes 1 and 2). P-HV backscatter also increased with shrub cover, but with more overlap between classes. Overlap was even greater in C-HV data (not shown).

Yucca-dominated sites (Class Y) had high backscatter in both L-HV and P-HV data, and could be confused with shrub-dominated sites if either L-HV or P-HV were used alone. However, yucca sites could be distinguished from non-yucca sites using these data in combination, because yucca sites had higher P-HV backscatter than non-yucca sites with similar L-HV backscatter.

The results might be explained by the greater sensitivity of longer wavelengths to larger canopy structural components (Ulaby *et al.*, 1986). P band appeared to be most sensitive to yucca, which has uniformly large-diameter stems (10-15 cm). L band appeared to be most sensitive to woody shrubs, which are intermediate in mean canopy element diameter between herbaceous vegetation (<1 cm) and yucca. Application of microwave backscattering models specifically developed for discontinuous canopies (e.g., Wang *et al.*, 1993) might reveal alternative explanations of the observed results.

4. REFERENCES

Buffington, L. C. and C. H. Herbel, 1965, "Vegetational Changes on a Semidesert Grassland Range from 1858 to 1963," *Ecological Monographs*, vol. 35, pp. 139-164.

Grover, H. D. and H. B. Musick, 1990, "Shrubland Encroachment in Southern New Mexico, U.S.A.: An Analysis of Desertification Processes in the American Southwest," *Climatic Change*, vol. 17, pp. 305-330.

Musick, H. B., 1984, "Assessment of Landsat Multispectral Scanner Spectral Indexes for Monitoring Arid Rangeland," *IEEE Transactions on Geoscience and Remote Sensing*, vol. GE-22, pp. 512-519.

Norikane, L., and A. Freeman, 1993, "*User's Guide to MacSigma0*," Jet Propulsion Laboratory Document D-10599, 147 p.

Pieper, R. D. and K. C. McDaniel, 1989, "Ecology and Management of Broom Snakeweed," *Snakeweed: Problems and Perspectives*, New Mexico Agricultural Experiment Station Bulletin 751, pp. 1-12.

Schlesinger, W. H., J. F. Reynolds, G. L. Cunningham, L. F. Huenneke, W. M. Jarrell, R. A. Virginia, and W. G. Whitford, 1990, "Biological Feedbacks in Global Desertification," *Science*, vol. 247, pp. 1043-1048.

Ulaby, F. T., R. K. Moore and A. K. Fung, 1986, *Microwave Remote Sensing Active and Passive, vol. III, From Theory to Applications*, Artech House, Norwood, Massachusetts, pp. 1884-1891.

Wang, Y., J. Day and G. Sun, 1993, "Santa Barbara microwave backscattering model for woodlands," *International Journal of Remote Sensing*, vol. 14, pp. 1477-1493.

Warren, P. L. and C. F. Hutchinson, 1984, "Indicators of Rangeland Change and Their Potential for Remote Sensing," *Journal of Arid Environments*, vol. 7, pp. 107-126.

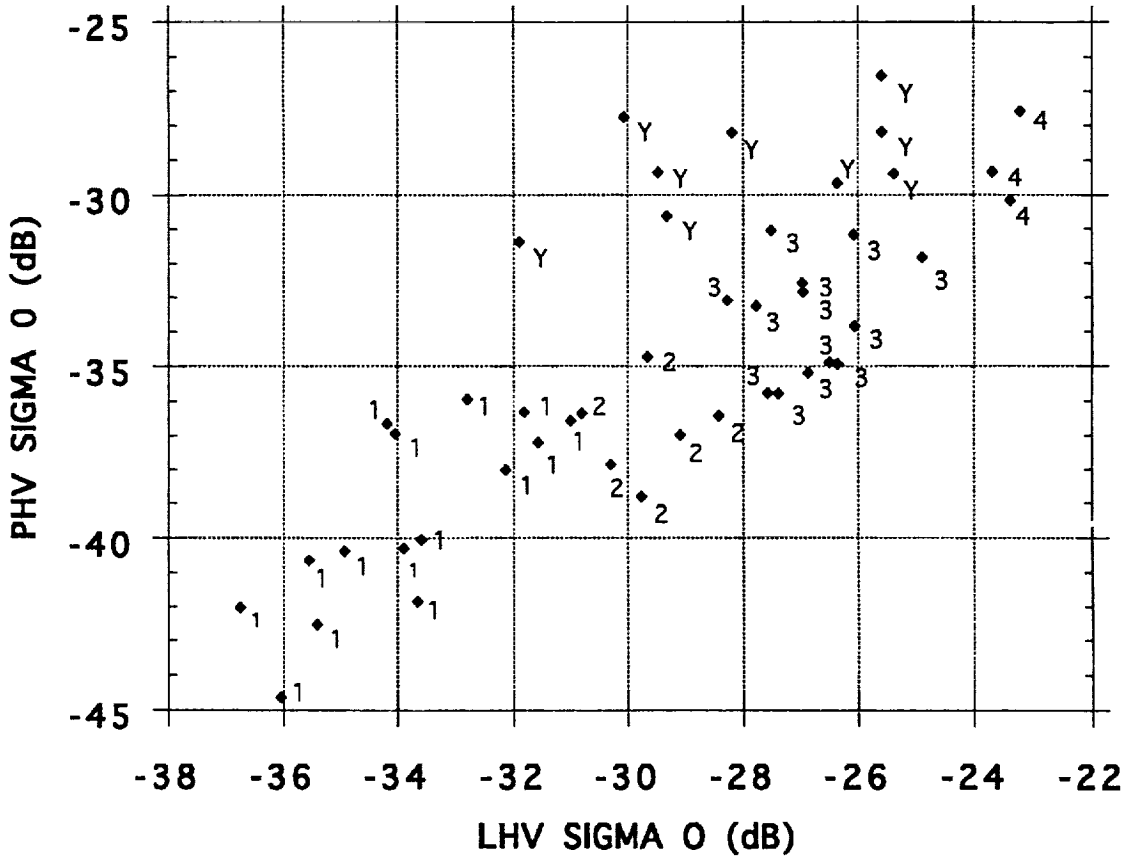

Figure 1. Backscattering coefficients (σ^0) in cross-polarized L and P bands for field sites. Y = yucca sites, 1-4 = woody shrub density classes as given in Table 1.

THE UNIQUE RADAR SCATTERING PROPERTIES OF SILICIC LAVA FLOWS AND DOMES

Jeffrey J. Plaut, Ellen R. Stofan
Jet Propulsion Laboratory
4800 Oak Grove Drive
Pasadena, CA 91109

Steven W. Anderson
Black Hills State University
Spearfish, SD 57799-9102

David A. Crown
Department of Geology and Planetary Science
321 Old Engineering Hall
University of Pittsburgh
Pittsburgh, PA 15260

1. INTRODUCTION

Silicic (silica-rich) lava flows, such as rhyolite, rhyodacite, and dacite, possess unique physical properties primarily because of the relatively high viscosity of the molten lava. Silicic flows tend to be thicker than basaltic flows, and the resulting large-scale morphology is typically a steep-sided dome or flow lobe, with aspect ratios (height/length) sometimes approaching unity. The upper surfaces of silicic domes and flows are normally emplaced as relatively cool, brittle slabs that fracture as they are extruded from the central vent areas, and are then rafted away toward the flow margin as a brittle carapace above a more ductile interior layer. This mode of emplacement results in a surface with unique roughness characteristics, which can be well-characterized by multi-parameter synthetic aperture radar (SAR) observations. In this paper, we examine the scattering properties of several silicic domes in the Inyo volcanic chain in the Eastern Sierra of California, using AIRSAR and TOPSAR data. Field measurements of intermediate-scale (cm to tens of m) surface topography and block size are used to assess the mechanisms of the scattering process, and to quantify the unique roughness characteristics of the flow surfaces.

2. GEOLOGIC SETTING

The Inyo volcanic chain represents the most recent eruptive activity (500-1200 years before present) in the Long Valley Caldera volcanic complex [Miller, 1985]. Deadman, Glass Creek, Obsidian, and Wilson Butte domes form a north-south trending chain of rhyolite flows, each 0.8 to 1.8 km in diameter, along the northwestern edge of the Long Valley Caldera. The lava textures include coarsely and finely vesicular pumice (CVP and FVP) and dense massive obsidian. CVP and obsidian are often associated with upwelling zones and "crease structures" [Anderson and Fink, 1992], while FVP is the dominant texture on most of the dome carapace. We have identified four distinct morphological units on the Inyo domes [Anderson et al., 1994]: 1) **Vent regions** are characterized by high relief, fractures and divergence of flow paths; 2) **Ridged areas** are characterized by regularly-spaced compressional ridges, with wavelengths between 10 and 15 meters and amplitudes of 1 to 4 meters; 3) **Jumbled regions** have more subdued topography and lack the characteristic structures present in vent and ridged areas; and 4) **Flow fronts** are the steep margins of the domes, with relief of tens of meters, and numerous nearly vertical cliff faces and zones of large blocky talus.

3. FIELD MEASUREMENTS

In order to understand the dominant mechanisms of radar scattering acting on the various surface units, topographic profiles at 25-cm intervals and boulder size

distributions were obtained at over 40 different vent, ridged, and jumbled zones on the Inyo dome surfaces [Plaut et al., 1994]. Examples are shown in Table 1. Data reduction of the topographic profiles included: detrending, rms height (standard deviation of surface heights), rms slope (standard deviation of point-to-adjacent-point slopes), and correlation length (offset for which autocorrelation function falls to 1/e). Boulder size distributions were obtained along each topographic transect; the transects were typically 20-40 meters in length.

4. AIRSAR AND TOPSAR DATA

The NASA/JPL AIRSAR instrument was flown over the Inyo site in the summer of 1993. Three passes (at 25, 35, and 45-degree incidence angles) were obtained in the standard polarimetric mode, and several passes were obtained in the TOPSAR C-band cross-track interferometric mode. Some AIRSAR data were also available from an earlier campaign in 1989. HH backscatter behavior at C- and L-band was analyzed and interpolated to simulate S-band (12 cm) for comparison with SAR data from lava domes on Venus thought to be of similar origin (Figure 1) [Pavri et al., 1992]. The Inyo domes show an overall higher backscatter and shallower scattering "law" slopes than the Venus domes, which is consistent with the extreme degree of roughness that is observed in the field on the surfaces of the Inyo domes. Circular polarization ratios were also analyzed to identify the relative contributions of single- and double-bounce scattering mechanisms. L-band circular polarization ratios as high as 0.75 were common on the dome surfaces.

A preliminary TOPSAR integrated processing run was conducted on one of the 1993 passes. After removal of a cross-track ramp, elevation values appear quite consistent with published conventional topographic data. C-band SAR data were ortho-rectified and backscatter cross-sections were corrected for the scattering area of tilted pixels. A map of local incidence angle was also produced. New lava flow volume calculations were made for two of the domes that appear to rest on a relatively level substrate: Wilson Butte (0.0018 km^3) and Obsidian Dome (0.0175 km^3).

5. DISCUSSION

Field measurements (Table 1) indicate that the surfaces of these silicic lava flows and domes are among the roughest ever measured. Rms height values commonly greater than 50 cm, and rms slope values commonly greater than 30 degrees, exceed those measured on all but the roughest a'a basaltic lava flows [Campbell and Garvin, 1993]. Blocks larger than 20 cm normally cover over 50% of the surface, suggesting that large-scale facets predominate over subwavelength scatterers in the SAR backscatter measurements. HH backscatter cross-sections are also among the highest ever measured for dry rock surfaces. TOPSAR scattering-area corrections should allow direct comparison of scattering behavior of various geologic surfaces independent of the local pixel-scale scattering angle, which could bias conventional measurements on high relief surfaces such as these. Circular polarization ratios approaching unity suggest a major contribution of double-bounce to the scattering process, which is consistent with the angular, blocky appearance of many of these surfaces in the field. Few unvegetated natural surfaces display the observed characteristics of very high, nearly isotropic backscatter and a high circular polarization ratio.

6. ACKNOWLEDGMENTS

The work described in this paper was carried out in part at the Jet Propulsion Laboratory, California Institute of Technology, under a contract with the National Aeronautics and Space Administration.

7. REFERENCES

Anderson, S.W., D.A. Crown, J.J. Plaut, and E.R. Stofan, 1994, "Surface characteristics of steep-sided domes on Venus and terrestrial silicic domes: A comparison," *Lunar and Planet. Sci. Conf. XXV*, 33-34.

Anderson, S.W., and J.H. Fink, 1992, "Crease structures: Indicators of emplacement rates and surface stress regimes of lava flows," *Geol. Soc. Am. Bul.* 104, 615-625.

Campbell, B.A., and J.B. Garvin, 1993, "Lava flow topographic measurements for radar data interpretation," *Geophys. Res. Lett.* 20, 831-834.

Miller, C.D., 1985, "Holocene eruptions at the Inyo volcanic chain, California - Implications for possible eruptions in the Long Valley Caldera," *Geology* 13, 14-17.

Pavri, B., J.W. Head, K.B. Klose, and L. Wilson, 1992, "Steep-sided domes on Venus: Characteristics, geologic setting, and eruption conditions from Magellan data," J. *Geophys. Res.* 97, 13445-13478.

Plaut, J.J., E.R. Stofan, D.A. Crown, and S.W. Anderson, 1994, "Topographic and surface roughness properties of steep-sided domes on Venus and Earth from radar remote sensing and field measurements," *Lunar and Planet. Sci. Conf. XXV*, 1091-1092.

Table 1. Roughness characteristics of selected lava flow surfaces from field measurements. Rms slopes for Venus domes are derived from Hagfors-modelled Magellan altimetry data.

Site	Rms Height, cm	Rms Slope, degrees	Correlation Length, cm	Arctan (h/l), degrees	Blocks, % < 10 cm	Blocks, % > 20 cm
Obsidian Dome, ridges	54.31	34.51	150.0	19.90	44	31
Osidian Dome, jumbled	30.09	35.52	50.0	31.04	10	64
Obsidian Dome, vent	82.29	40.01	125.0	33.36	7	73
Obsidian Dome, slabs	50.86	23.76	200.0	14.27	31	50
Cima, a'a channel	32.49	22.33	400.0	4.64	50	26
Cima, a"a margin	53.18	32.68	175.0	16.90	28	51
Kilauea, pahoehoe[1]	7.70	3.92	350.0	1.27		
Venus, steep-sided domes[2]		<5.0				

[1]from Campbell and Garvin (1993) [2]from Pavri et al. (1992)

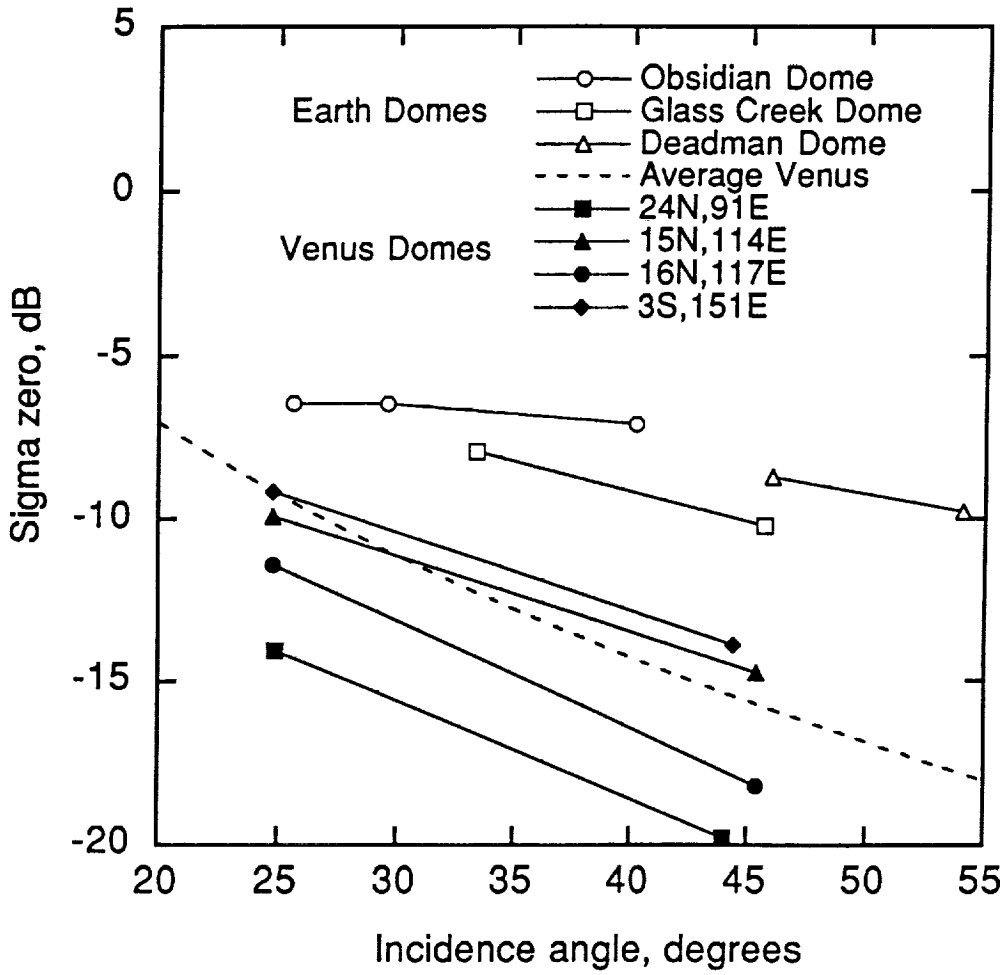

Figure 1. HH SAR backscatter as a function of incidence angle for the Inyo domes and similar features observed on Venus by Magellan. AIRSAR C- and L-band data are interpolated to simulate Magellan's S-band. Backscatter behavior indicates distinct differences in surface roughness of the Venus and Earth domes.

On the Potential of Long Wavelength Imaging Radars for Mapping Vegetation Types and Woody Biomass in Tropical Rain Forests

Eric J. Rignot, Reiner Zimmermann and Ram Oren

Jet Propulsion Laboratory, California Institute of Technology, Pasadena, CA 91109

Ph (818) 354-1640; Fax (818) 393-6943

1. STUDY SITE AND BIOMASS ESTIMATES

The Manu National Park, in Peru, is located at the remote western edge of the Amazon basin [1-3]. It contains pristine, tropical rain forest types with a striking diversity of tropical tree species. The generally humid climate is interrupted by a dry season in July-August. Floodplain succession and climax forests occur on nutrient rich alluvial soils along the Rio Manu and mature forests on more dry and leached soils on the adjacent hills. Since a biomass inventory was not available for any forest in this area, a ground team characterized the major forest types and approximate spatial distribution of vegetation along the accessible areas of the lower Manu river in September 1993. Seventeen plots with representative vegetation types were measured for average tree and canopy height, canopy closure, tree density and understory composition. The aboveground biomass for all forest types was estimated by applying allometric equations [4], derived from pristine South-Asian forests [5]. Aboveground dry biomass of early forest succession like mature *Tessaria integrifolia* (Asteraceae) and *Gynerium sagittatum* (Poaceae) (10 m) was estimated to be 4 kg/m^2 and 4.3 kg/m^2 in *Gynerium-Cecropia membranacea* stand (17 m). Aboveground biomass in a permanently inundated Aguajal (max. 22 m height) was estimated to be 13 kg/m^2, in a mainly dry and open Aguajal (26 m) 17 kg/m^2, and 18 kg/m^2 in a typical Aguajal (28 m) with moist soil and a high palm density. Broadleaf forest types along the Rio Manu are evergreen to semi-deciduous with wide variations in canopy structure. In the floodplain, we calculated for a mosaic forest (>27 m) on rich alluvial soil a biomass of 31 kg/m^2. On adjacent hills, forests vary from tall stands with closed canopies to open semi-deciduous stands. We calculated 28 kg/m^2 for a semi-deciduous upland forest (30 m) and 46 kg/m^2 for a tall forest (40 m) with closed overstory. Total aboveground biomass of a tall (>50 m), old growth floodplain forest at Cocha Cashu, Rio Manu, was estimated to be 104 kg/m^2. This value represents probably the highest aboveground biomasss accumulation found in this area due to the large size of individual trees reaching emergent tree heights of 53 m with diameter at breast height (dbh) of 3 m and a closed canopy of dominant trees with dbh between 0.9 and 2.4 m [6]. The estimated biomass values for mature old growth floodplain forest clearly exceed the reported average value of 67 kg/m^2 for high dense tropical forests of the generally poorer soils on Terra Firme in the Brazilian forests [7]. However, in general, even higher forest volumes are possible and have been repeatedly reported for temperate coastal rain forests in higher latitudes [8]. Since the impressive, mature floodplain forests cover relatively small areas, the average aboveground biomass weighed by the area covered by each species is expected to be much lower.

2. MAPPING OF MAJOR VEGETATION FORMATIONS

Using a maximum-a-posteriori Bayesian classifier for polarimetric SAR data, and selecting training areas representative of various types of vegetation along the Rio Manu floodplain, we generated a classification map (AIRSAR Workshop Slide 2b) of the 10-km wide P-band data into the following 9 categories of land cover: 1) tall semi-deciduous forest; 2) palm aguajal; 3) tessaria forest; 4) gynerium forest; 5) cecropia forest; 6) mosaic forest; 7) segdes; 8) bare soil; and 9) water. Classifications obtained using the L- or C-band data did not prove as useful as the one generated using the P-band data. At P-band, HH-polarization is the most useful polarization for separating the different types of vegetation. Comparison of the SAR results with sample plots placed at selected locations along the Manu river indicates that the SAR-derived vegetation map provides a correct representation of the distribution in forest types in that area, and that the P-band radar is able to separate most major vegetation formations in the floodplains. The treatment of forested areas in the uphill section of the Park is complicated by the presence of an undulating 30-50 m topography, for which we do not have a reliable digital elevation model, and which would need to be accounted for to obtain a correct mapping of the vegetation.

3. MAPPING OF MAJOR CLASSES OF BIOMASS

We developed an empirical relationship between forest biomass and radar backscatter for this area to generate a map of forest biomass [9]. At the low biomass levels (< 10 kg/m^2), we used the regression curve which was developed for Alaskan forests and which utilized the P-band HH-, HV-, and VV-polarized data gathered during the dry season [10]. At the higher biomass levels, the regression curve correctly separated the different classes of biomass, but underestimated forest biomass quite significantly. We modified the regression to increase the predicted biomass levels for large radar backscatter values and obtain a better agreement with our ground estimates.

Areas where the forest biomass predicted from the radar exceeds 30 kg/m^2 (dark green) correspond to the mature floodplain forests where woody biomass is indeed expected to be the largest. The forest floor in the imaged broadleaf forests was dry at the time of the AIRSAR overflight (the dry season ends in September), so the enhanced radar signature of these stands at HH-polarization is not caused by wetter ground layers but more likely by tall tree trunks of large diameter. Forest biomass is lower in palm forests (green), which are surrounded by broadleaf forests of higher biomass (dark green). Old meanders, sealed off by freshly deposited sediment and showing as oxbow lakes (Cochas) with open water are mapped as areas of no biomass (black). Low biomass (brown) is estimated along the termini of Cochas, having an early succession of sedges, grasses and shrubs (especially *Annona tessmannii* (Annonaceae)), which are occasionally intercut by a tall stand of *Heliconia episcopalis* (Musaceae) with slightly larger biomass (oxbow at center right of the scene, green). In the expanding meander loop, in the center left of Slide 2b, that points down towards the lower border of the river, the early succession of riparian vegetation is well discriminated in the biomass map. Forest succession starts from the beach with short, even-aged stands of fast-growing *Tessaria* shrubs, followed by *Gynerium* stands (6 m in height) with higher biomass (dark brown). Adjacent are older successional stages of *Tessaria-Gynerium* (10-12 m in height) (light brown), and pure *Gynerium* (yellow). Continuing inland, towards the top of the scene, are deciduous leafless tree species

mixed with *Cecropia* (10-26 m) above a 5 m tall understory of *Gynerium*. This forest appears blue-green in AIRSAR Workshop Slide 2a, and corresponds to a higher biomass level. A mosaic of semi-deciduous floodplain forest (30-35 m) with higher predicted biomass follows. This type of clearly zoned and highly productive, riparian forest succession, where each stage reaches a greater absolute height than the previous one, is characteristic of this area and can be identified at many other locations along the river in AIRSAR Workshop Slide 2a.

4. CONCLUSIONS

In the tropical rain forests of Manu, in Peru, where forest biomass ranges from 4 kg/m^2 in young forest succession up to 100 kg/m^2 in old, undisturbed floodplain stands, the P-band polarimetric radar data gathered in June of 1993 by the AIRSAR instrument separate most major vegetation formations and also perform better than expected in estimating woody biomass. The worldwide need for large scale, updated biomass estimates, achieved with a uniformly applied method, as well as reliable maps of land cover, justifies a more in-depth exploration of long wavelength imaging radar applications for tropical forests inventories.

Acknowledgements This work was carried out at the Jet Propulsion Laboratory, California Institute of Technology, under a contract with the National Aeronautics and Space Administration. The authors would like to thank John Terborgh, Sharon Billings, Bruce Chapman, and Viviana Horna-Rodriguez for help in getting the ground truth data in Peru.

References

[1] Terborgh, J., *Five New World Primates: A study in Comparative Ecology*, Princeton University Press, Princeton, NJ, 1983.

[2] Terborgh, J., Habitat selection in Amazonian birds. In *Habitat Selection in Birds* (Ed. M.L. Cody), Academic Press, New York, pp. 311-318, 1985.

[3] Kalliola R., J. Salo and Y. Mäkinen, Regeneracion natural de selvas en la Amazonia Peruana 1: dinamica fluvial y sucesion ribereña. *Memorias del Museo de historia Natural 'Javier Prado'* (Lima), 18, pp. 1-102, 1987.

[4] Ogawa, H., K. Yoda, K. Ogina and T. Kira, Comparative ecological studies on three main types of forest vegetation in Thailand II. Plant biomass, *Nature and life in S.E. Asia* 4, pp. 49-80, 1965.

[5] FAO-UNESCO-UNEP. Tropical forest ecosystems. Chapter 10. Gross and net primary production and growth parameters, pp. 233-248, 1978.

[6] Tosi, J.A., Zonas de vida natural en El Peru, Instituto Interamericano de Ciencias Agricolas de la OEA Zona Andina, Boletin Tecnico 5, p. 271, 1960.

[7] Fearnside, P.M., L. Niwton and F. M. Fernandes, Rain forest burning and the global carbon budget: biomass, combustion efficiency, and charcoal formation in the Brazilian Amazon, *J. Geophys. Res.*, 98, pp. 16733-16743, 1993.

[8] Walter, H. and S.W. Breckle, Ecological systems of the Geobiosphere 4, Temperate and polar biomes other than northern Eurasia. Springer Verlag, Berlin, 1991.

[9] Rignot, E., R. Zimmerman, J.J. van Zyl and R. Oren, Spaceborne applications of P-band imaging radars for measuring forest biomass, *IEEE Trans. on Geosc. and Rem. Sens.*, submitted, 1994.

[10] Rignot, E., C. Williams, J.B. Way and L. Viereck, Radar Estimates of Aboveground Biomass in Boreal Forests of Interior Alaska, *IEEE Trans. on Geosc. and Rem. Sens.*, 32, pp. 1117-1124, 1994.

LITHOLOGIC CONTROLS ON AIRSAR SIGNATURES OF BEDROCK AND ALLUVIUM, AT LUNAR CRATER, NEVADA

Benoit Rivard, Marc D'Iorio, and Paul Budkewitsch

Canada Centre for Remote Sensing, Applications Division, 588 Booth St., Ottawa, Canada, K1A 0Y7.

1. INTRODUCTION

Radar backscatter intensity as measured by calibrated synthetic aperture radar (SAR) systems is primarily controlled by three factors: local incidence angle, wavelength-scale roughness, and dielectric permittivity of surface materials. In order to make adequate use of radar observations for geological investigations of surface type, the relationships between lithology and the above characteristics must be adequately understood. In arid terrains weathering signatures (e.g. fracturing, debris grain size and shape, slope characteristics) are controlled to some extent by lithologic characteristics of the parent bedrock. These textural features of outcrops and their associated debris control radar backscatter to varying degrees. The quad-polarization JPL AIRSAR system allows sampling of textures at three distinct wavelength scales: C-band (5.66 cm), L-band (23.98 cm), and P-band (68.13 cm).

This paper presents a discussion of AIRSAR data using recent field observations of weathered felsic and basaltic volcanic rock units exposed in the southern part of the Lunar Crater Volcanic Field, in the Pancake Range of central Nevada (Snyder et al, 1972). The focus is on the relationship of radar backscatter at multiple wavelengths to weathering style and parent bedrock lithology.

2. GEOLOGIC SETTING

The Lunar Crater portion of the Pancake Range consists of Tertiary (31 to 25 my old) rhyolitic to andesitic volcanic rocks (Ekren et al. 1974) including andesitic and quartz latitic lavas, and a number of distinct welded and bedded tuff units displaying varying phenocryst and lithic contents and devitrification textures (Snyder et al, 1972). Basin and Range style tectonics strongly faulted the Tertiary volcanics and also isolated the drainage of the region. Nearby Lunar Lake playa is the result of this internal drainage. Pleistocene and Holocene basalt units extruded through a number of cones and NNE trending fissures (Scott and Trask, 1971; Snyder et al, 1972). The region has remained relatively stable during the Quaternary. Mass wasting has resulted in the development of extensive alluvial fans, and fluvial deposits, and recent aeolian activity has locally developped desert pavement.

Basalt outcrops in the area show relatively mature upper weathered surfaces, with well-developed desert pavements consisting of basalt cobbles 10-40 cm in diameter resting on an aeolian-derived soil of up to several meters in thickness. Felsic outcrop morphologies are highly variable, ranging from low rounded hills with relatively thick soils to cap-rocked mesas with fresh bedrock exposures and steep cliff faces as high as 250 m. Alluvial deposits are predominantly sandy gravels, although several washes contain large boulders reflecting high-energy depositional environments.

3. FIELD OBSERVATIONS

Within the area, two types of terranes were the focus of field observations. The first is a plateau occupied by a flat lying rhyolite ashflow exposed largely as in-situ debris.The top few metres of the ashflow are strongly welded and dissected into metre-sized columnar joints. Their weathering products form three domains with distinct surface morphologies: i) metre-size boulders (core stones) and large exposures of spheroidally weathered bedrock with dispersed Juniper trees, ii) areas of cm-size debris with sparsely dispersed shrubs and, iii) areas of decimetre-size slabs with sparsely dispersed shrubs. All three domains display unique SAR

signatures and as a whole are characteristic of the upper most part of the ashflow. Immediately below the columnar joints is a more fractured and friable part of the ashflow which is exposed along the valleys dissecting the plateau. This surface is characterised by loose cm-size debris overgrown by denser and larger shrubs than observed at the top of the plateau. Table 1 summarize the characteristics of the unconsolidated material and vegetation for both parts of the ashflow. The controls on the SAR signals by surface characteristics are discussed below.

The second terrain consists of alluvial fans with older areas of desert pavement dissected by active channels. The fans material varies in lithological makeup and surface roughness depending on provenance. The majority of clasts are derived from felsic ashflows, which is the bedrock for most of the mesas, making the field determination of clast provenance a difficult task. Locally, however, fan surfaces displaying subtle differences in average clast size due to specific source regions can be seen in the SAR data. Table 2 provides a description of fan surfaces which are difficult to separate in the field but which can be distinguished using the polarimetric SAR signatures.

4. DATA ANALYSIS

Alluvial fans

HH and VV polarizations

The mapping of alluvial fans was conducted using C-band data because of its sensitivity to the range of clast sizes dominant on these surfaces (0.5-1.5 cm). The effect of surface roughness on C_{HH} and C_{VV} returns is very strong particularly in the case of smooth surfaces (rms surface heights less than 1 cm). Subtle differences in mean clast size, in this case 0.5 cm and 1.5 cm, are detectable and can be related to the provenance of the material in the fans. L and P-band images did not improve the mapping of most fans but did outline portions of fans dominated by boulders deposited in a high-energy environment.

The drainage channels cutting the fans are imperceptible in C band. The channels are dominated by sand and thus are smoother than surrounding fans but these differences in roughness are not detectable because the channels are subpixel in size. The channels are easily observed in L and P band wavelengths because the presence of moisture at depth (< 4 cm) is detectable resulting in enhanced backscatter.

HV polarization

Images of the cross-polarized signals portray information largely related to the distribution of vegetation density and type (or size). Fan areas occupied by grass are distinct and show the weakest signals at all bands. Fan areas with shrub density (< 15%) and size (diameter < 35 cm) such as described in table 2 produce weak signals and signal variations in C band. Distinct signatures in C and L band were observed for a site with 30% shrubs with average crown diameter of 45 cm. This extent of vegetation cover is easily mapped using a combination of C_{HV}, L_{HV} and P_{HV} and is typical of widespread fan areas located in the downslope proximity of the plateaus. The vegetation on the fans contributes minimal HH and VV returns and does not mask the fan roughness variations observed on the like-polarization images.

Plateau

HH and VV polarizations

Although mapped by Snyder et al (1972) as a single map unit, the two subunits of the ashflow described in table 1 display dramatically different radar signatures related to weathering style. These two units illustrate the use of radar for lithologic discrimination based on surface roughness and vegetation. Unit 1 forms an erosional cap to the mesa and is characterized by a predominance of rock debris. The three geomorphic domains of unit 1 span a range of surface roughness from smooth bedrock surfaces and relatively smooth pebble pavement to irregular surfaces rich in rock slabs. These surfaces respectively produce stronger returns in C and P band. Rock outcrops with steep topography provide strong returns independent of wavelengths. In contrast unit 2 shows high returns in C and L-band where significant L-band return from the woody component of the shrubs appears to be contributed to the return of the fine pebble surface.

HV polarization

Large, 2-3 m high, Juniper trees produce strong returns in P-band, a radar signature diagnostic of unit 1. Unit 2 produces strong returns in L band because of the high concentration of relatively large sagebrushes and saltbushes which have thick, woody stems and branches (table 2).

5. CONCLUSIONS

For the southern Lunar Crater Volcanic Field, analysis of SAR imagery and field observations indicates that the radar signatures of alluvial fan surfaces and weathered bedrock are largely controlled by surface roughness and the nature of the vegetation cover. Because these characteristics vary with lithology, it is possible to use the frequency and polarimetric information to map lithology and alluvial fans.

In this site we were able to successfully separate 3 types of alluvium in the depositional flat based on a combination of roughness scale and vegetation type. These characteristics appear to be related to material provenance.

On the plateau, we were able to discriminate different weathering styles of the same lithology, which are indicative of different levels (depths) of erosion within the ashflows. We are presently evaluating whether variations in weathering styles within an ashflow can be related to variations in degree of welding.

6. REFERENCES

Ekren, E., W. Quinlivan, R. Snyder, and F. Kleinhampl, 1974, Stratigraphy, structure, and geologic history of the Lunar Lake caldera of Northern Nye county, Nevada, Journal Research U.S. Geological Survey 2(5), pp. 599-608.

Scott, D.H. and N.J. Trask, 1971, Geology of the Lunar Crater Field, Nye County, Nevada, USGS Prof. paper 599-I.

Snyder, R.P., E.B. Ekren and G.L. Dixon, 1972, Geologic map of the Lunar Crater quadrangle, Nye County, Nevada, USGS Misc. Inv. Map I700.

7. TABLES

Table 1. Surficial characteristics of the ashflow plateau

Unit 1(mostly derived from columnar joints):

- Domain 1 (fig. 1, left of letter a): bedrock displaying granite weathering, 5-10%* cover of juniper trees 3 m in height with average trunk diameter of 7-12 cm.
- Domain 2 (fig. 1, left of letter b): pavement of densily packed 1-2 cm size rounded fragment, 20% shrubs averaging 50 cm in height and 30 cm in diameter. Maximum branch diameter of 1-2 cm.
- Domain 3 (fig. 1, left of letter c): pavement of flat slabs with an average area of 25 x 25 cm and up to 50 x 100 cm, which occupy approximately 23% of the surface, and set in a matrix of 0.5-1.5 cm size angular clasts. Vegetation is similar to that observed in domain 2.

Unit 2 :

- The unit (fig. 1, below letter d) consists of a loose surface, 2-3 cm deep, made up of fine rubble (0.5-2 cm in size) covered to 30-40% by sage shrubs. Shrubs are in average 1m in height, 0.75m in diameter, with a trunk diameter of 6 cm.

*Refers to estimates in plane view

Table 2. Surficial characteristics of the alluvial fans

- Fan 1 (fig. 1, letter e): 5-10% grass, 8% shrubs with an average diameter of 25 cm. Remainder is a weakly compacted surface two thirds of which are clast < 0.5 cm in size and one third of which are fines (< 1mm).

- Fan 2 (fig. 1, letter f): 15% shrubs with an average diameter of 35 cm and trunk size of 1-2 cm. The remainder is a compacted surface largely dominated (< 90%) by rounded clasts of uniform size (1-1.5 cm).

- Channels consist dominantly of loose sand (beyond a decimeter) with few cm clasts and rare boulders. Moisture was present at 4cm depth and vegetation is vigorous. Bushes are typically 50cm in height.

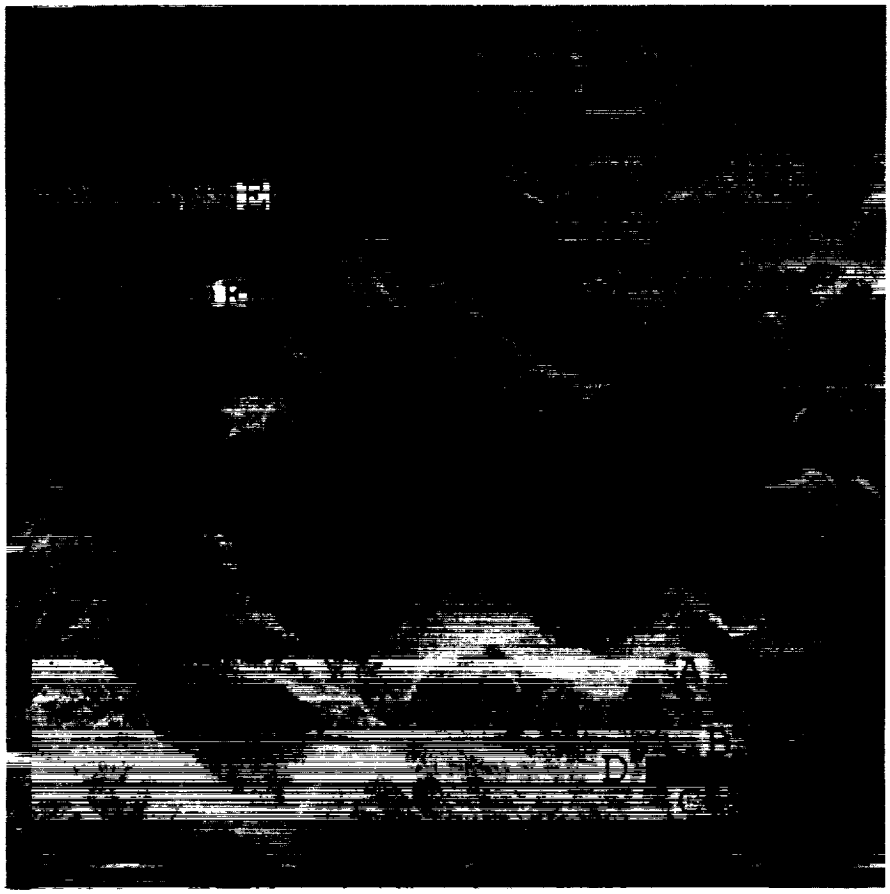

Figure 1. AIRSAR C-band HH image in slant range, illumination from the top (northwest). Calibration of phase, amplitude and co-channel gain imbalance was conducted using trihedral corner reflectors and assuming the absence of relief. No attempt was made to calibrate the data with the use of a DEM. Thus our efforts have focused on the analysis of SAR signatures for relatively flat areas. Approximate scene dimensions of 9 x 9 km. Letters refer to locations discussed in the text and described in the tables.

Estimation of Penetration of Forest Canopies by Interferometric SAR Measurements

Ernesto Rodriguez, Thierry R. Michel
Jet Propulsion Laboratory
California Institute of Technology
4800 Oak Grove Drive, MS 300-319
Pasadena, California 91109
Phone: (818)354-5668, Fax: (818)393-5184, e-mail:er@dionysus.jpl.nasa.gov

and David J. Harding
Goddard Space Flight Center, Greenbelt, Maryland

In contrast to traditional Synthetic Aperture Radar (SAR), an Interferometric SAR (INSAR) yields two additional measurements: the phase difference and the correlation between the two interferometric channels. The phase difference has been used to estimate topographic height. For homogeneous surfaces, the correlation depends on the system signal-to-noise (SNR) ratio, the interferometer parameters, and the local slope. In the presence of volume scattering, such as that encountered in vegetation canopies, the correlation between the two channels is also dependent on the degree of penetration of the radiation into the scattering medium. In this paper, we propose a method for removing system and slope effects in order to obtain the decorrelation due to penetration alone. The sensitivities and accuracy of the proposed method are determined by Monte Carlo experiments, and we show that the proposed technique has sufficient sensitivity to provide penetration measurements for airborne SAR systems.

Next, we provide a theoretical model to estimate the degree of penetration in a way which is independent of the details of the scattering medium. We also present a model for the correlation from non-homogeneous layers. We assess the sensitivity of the proposed inversion technique to these inhomogeneous situations. Finally, we present a comparison of the interferometric results against in situ data obtained by an airborne laser profilometer which provides a direct measurement of tree height and an estimate of the vegetation density profile in the forested areas around Mt. Adams, WA.

ACKNOWLEDGMENT

The research described in this paper was performed by the Jet Propulsion Laboratory, California Institute of Technology, under a contract with the National Aeronautics and Space Administration and with the Advanced Research Projects Agency (ARPA).

N95-33815

Regional Mapping of Forest Canopy Water Content and Biomass Using AIRSAR Images Over BOREAS Study Area

Sasan Saatchi, Eric Rignot, Jakob van Zyl
Jet Propulsion Laboratory
Pasadena, CA 91109
tel: (818) 354-1051, fax: (818) 393-6943
E-mail: saatchi@bacchus.jpl.nasa.gov

In recent years, monitoring vegetation biomass over various climate zones has become the primary focus of several studies interested in assessing the role of the ecosystem responses to climate change and human activities. Airborne and spaceborne Synthetic Aperture Radar (SAR) systems provide a useful tool to directly estimate biomass due to its sensitivity to structural and moisture characteristics of vegetation canopies. Even though the sensitivity of SAR data to total aboveground biomass has been successfully demonstrated in many controlled experiments over boreal forests and forest plantations, so far, no biomass estimation algorithm has been developed. This is mainly due to the fact that the SAR data, even at lowest frequency (P-band) saturates at biomass levels of about 200 tons/ha, and the structure and moisture information in the SAR signal forces the estimation algorithm to be forest type dependent.

In this paper, we discuss the development of a hybrid forest biomass algorithm which uses a SAR derived land cover map in conjunction with a forest backscatter model and an inversion algorithm to estimate forest canopy water content. It is shown that unlike the direct biomass estimation from SAR data, the estimation of water content does not depend on the seasonal and/or environmental conditions. The total aboveground biomass can then be derived from canopy water content for each type of forest by incorporating other ecological information. Preliminary results from this technique over several boreal forest stands indicate that 1) the forest biomass can be estimated with reasonable accuracy, and 2) the saturation level of the SAR signal can be enhanced by separating the crown and trunk biomass in the inversion algorithm.

We have used the JPL AIRSAR data over BOREAS southern study area to test the algorithm and to generate regional scale water content and biomass maps. The results are compared with ground data and the sources of errors are discussed. Several SAR images in synoptic modes are used to generate the parameter maps. The maps are then combined to generate mosaic maps over the BOREAS modeling grid.

This work was carried out at the Jet Propulsion Laboratory, California Institute of Technology and Goddard Space Flight Center under a contract with the National Aeronautics and Space Administration.

N95-33816

APPLICATION OF IEM MODEL ON SOIL MOISTURE AND SURFACE ROUGHNESS ESTIMATION

Jiancheng Shi
Center for Remote Sensing and Environmental Optics
University of California, Santa Barbara

J. R Wang, P. E. O'Neill, A. Y. Hsu, and E. T. Engman
NASA/GSFC
Hydrological Sciences Branch

ABSTRACT

Monitoring spatial and temporal changes of soil moisture are of important to hydrology, meteorology, and agriculture. This paper reports a result on study of using L-band SAR imagery to estimate soil moisture and surface roughness for bare fields. Due to limitations of the Small Perturbation Model, it is difficult to apply this model on estimation of soil moisture and surface roughness directly. In this study, we show a simplified model derived from the Integral Equation Model for estimation of soil moisture and surface roughness. We show a test of this model using JPL L-band AIRSAR data.

INTRODUCTION

Estimates of soil moisture are of great importance in numerous environmental studies, including hydrology, meteorology, and agriculture. In spite of its importance, soil moisture data is not generally used in resource monitoring or prediction because they are difficult and costly to measure on a routine basis over large areas.

Our previous work (Shi, 1992) indicated that the ratio of the co-polarization signals could be used for soil moisture retrieval at longer wavelengths (L-band) and at larger incidence angles ($> 40°$). The algorithm to infer soil moisture from imaging radar data was based on a first-order surface scattering model - the Small Perturbation model. This model predicts that the co-polarization ratio is sensitive to soil moisture at large incidence angles but not to surface roughness. However, due to the surface roughness parameters of most of natural surface are outside the range of the valid conditions for the Small Perturbation and Geometric Optical models, application of these surface scattering models are greatly limited to certain types of the surface roughness conditions. This results in an underestimation of soil moisture when the first-order Small Perturbation model was applied to imaging radar data.

The recently developed Integral Equation Model (IEM) (Fung, 1992) allows a much wider range of the surface roughness conditions, making it possible to estimate soil moisture using IEM model. However, it does not allow to apply this model directly to infer geophysical parameters because of the complicity of this model and the limited independent observations provided by SAR measurements.

Washita '92 was a cooperative experiment between NASA, USDA, several other government agencies and universities with the objective of testing the usefulness of remotely sensed data in hydrologic modeling. During the experiment, a time series of spatially distributed hydrologic data, focusing on soil moisture and evaporative fluxes, using both conventional and remotely sensed methods, were collected over the Little Washita Watershed and a few immediately surrounding areas in Chickasha, OK. Data collection was conducted during the period of June 10 through June 18, 1992. The observations followed a period of very heavy rains over several weeks that ended on June 9 provided saturated soil conditions with standing water at the beginning of the experiment. No rainfall occurred during the experimental period thus allowing the observation of drying conditions. NASA provided support for two aircraft; the

C-130 and the DC-8. The DC-8 flew the three frequency synthetic aperture radar which provided data for this analysis. Figure 1 shows two L-band VV/HH ratio images, where the brightness is proportional to soil moisture at a given incidence angle and inversely related to the surface roughness parameter, taken on June 10 and 18, 1992 of the study site - the Little Washita Watershed.

This study shows our continue efforts on developing and testing the algorithm for retrieval soil moisture and roughness parameters using L-band JPL AIRSAR data. We show (1) a simplified surface backscattering model particularly derived for soil moisture conditions with a random rough surface from the numerical simulations by IEM model, and (2) soil moisture retrieval model test and comparison with ground measurements using L-band AIRSAR data.

INTEGRAL EQUATION MODEL SIMPLICATION

The surface backscattering is a function of the permittivity of soil and the roughness of the air-soil interface which is described by the auto-correlation function of random surface height, the standard deviation of the surface height, and the correlation length. Due to the surface roughness parameters of most of natural surface are outside the range of the valid conditions of the tradition surface scattering models, such as the Small Perturbation and Geometric Optical models, application of these surface scattering models are greatly limited to certain types of the surface roughness conditions. The recently developed Integral Equation Model (IEM) (Fung, 1992) allows a much wider range of the surface roughness conditions.

Due to complicity of IEM model and the limited number of independent observations from the polarimetric SAR, we need to minimize or combine these factors in order to separate the effects of the surface roughness and the dielectric constant of soil. As shown by Fung (1992), when the random surface height s is small, I^n_{pp} can be approximated to α_{pp} which reflectivity function of the Small Perturbation Model. This makes it possible to simplify IEM model for a relative smooth surface. Using IEM model, we simulated the surface backscattering coefficients of σ^{vv}, σ^{hh}, and σ_s^{vvhh*} at L-band for the most common soil moisture and surface roughness conditions. The simulated backscattering coefficients cover the ranges for soil moisture from 5 percent to 50 percent by volume at interval 5 percent, for the incidence angle from 20° to 70° at interval 5°, for the standard deviation of random surface height from 0.2 cm to 3.0 cm at interval 0.2 cm, and for the surface correlation length 2.5 cm to 25 cm at interval 2.5 cm. The total simulated backscattering coefficients is 23,475 for different combinations of incidence angle, soil moisture and surface roughness parameters.

Through statistical analysis, we found a simplified form for the backscattering coefficients

$$\sigma_{pp} = |\alpha_{pp}|^2 \left[\frac{Sr}{(a_{pp}(\theta_i) + b_{pp}(\theta_i)Sr)}\right] \tag{1}$$

and the ratio of σ_{hh} to σ_{vv}

$$\frac{\sigma_{hh}}{\sigma_{vv}} = \frac{|\alpha_{hh}|^2}{|\alpha_{vv}|^2} exp[a_r(\theta_i) + ks(b_r(\theta_i) + c_r(\theta_i)W)] \tag{2}$$

where pp represents polarization. Sr, which is $Sr = (ks)^2W$. W is the Fourier transform of the power spectrum of the surface correlation function. a_{pp}, b_{pp}, a_r, b_r, and c_r are the coefficients only depending only on the incidence angle and polarization.

As shown in Figure 2 for σ_{vv} and $\frac{\sigma_{hh}}{\sigma_{vv}}$, the simplified model agrees well with the IEM model for the simulated conditions. For VV polarization, the maximum absolute error between the IEM model and the simplified model is 1.2 dB and the absolute error within 0.23 dB can be obtained with 95 percent confidance interval. For the ratio, the maximum absolute error is 0.89 dB and 0.17 dB for 95 percent confidance interval.

Notice that there are three unknowns in the IEM model: the dielectric constant, random surface height, and correlation length. The simplified model in Equation (1), has only two unknowns the dielectric constant through the reflectivity $|\alpha_{pp}(\theta, \epsilon)|$ and the surface roughness parameter Sr. When

we use two polarization measurements, both the dielectric constant ϵ and surface roughness Sr can be solved simultaneously. The task is to select the best pair of the simplified backscattering model for different polarizations. We have evaluated all pairs of σ_{vv}, σ_{hh}, and σ_{vvhh} and their linear combinations. We found that the best pair is σ_{vv} and σ_{vvhh}. Using two of Equations of (1) for σ_{vv} and σ_{vvhh}, we found the relationship:

$$\frac{|\alpha_{vv}|^2}{\sigma_{vv}} = a_{vx}(\theta_i)\frac{|\alpha_{vvhh}|^2}{\sigma_{vvhh}} + b_{vx}(\theta_i) \tag{3}$$

Using Equation (3), we can infer soil moisture directly by varying the dielectric constant through $|\alpha_{vv}|^2$ and $|\alpha_{vvhh}|$. The $a_{vx}(\theta_i)$ and $b_{vx}(\theta_i)$ are coefficients pre-determined from statistical analysis. Then, the surface roughness parameters ks and W can be found by using Equations (1) and (2).

ESTIMATE SOIL MOISTURE USING AIRSAR

To perform the algorithm for measuring soil moisture and surface roughness parameter the stokes matrix was determined by the mean value within a 3 × 3 window in order to reduce the effect of image speckle. In addition to the model simplification, image speckle, antenna thermal noise and the calibration error will also decrease the measurement accuracy. We expect that the measurement of soil moisture and surface roughness parameter can not be done for some pixels and that some degree of uncertainty exists in the estimated soil moisture surface roughness parameter. In post-processing, an average value from surround pixels within a 5 × 5 window was applied to reduce the uncertainties.

Figure 3 on top and bottom show three images of the inferred soil moisture, ks, and W from AIRSAR data-take on June 10, and 18, 1992, respectively. The image brightness is proportion to the soil moisture, ks, and W. The black regions in Figure 3 are the SAR measurements outside surface scattering model predictions, such as vegetation covered fields. The field measurements indicated that there was a significant drop of soil moisture from 28.7 the inferred soil moisture from SAR measurements. Figure 3 on middle and right show the images of the inferred surface roughness parameters: ks and W. They are almost constant for the bare fields except the vegetated fields. Those vegetations may cause significant scattering contribution, especially at large incidence angle, which affects both the backscattering magnitudes and the difference between two polarizations. As a result it will underestimate soil moisture and over-estimate surface roughness parameters.

REFERENCES

J. Shi, J. van Zyl, J. V. Soares, and E. T. Engman. "Development of soil moisture retrieval algorithm for L-band SAR measurements," *Proceedings IGARSS '92* , IEEE no 92CH3041-1, pp 495–497, 1992.

A. K. Fung, Z. Li, and K. S. Chen. "Backscattering from a randomly rough dielectric surface," *IEEE Trans. Geosci. Remote Sens.*, vol 30, no 2, pp 356-369, 1992

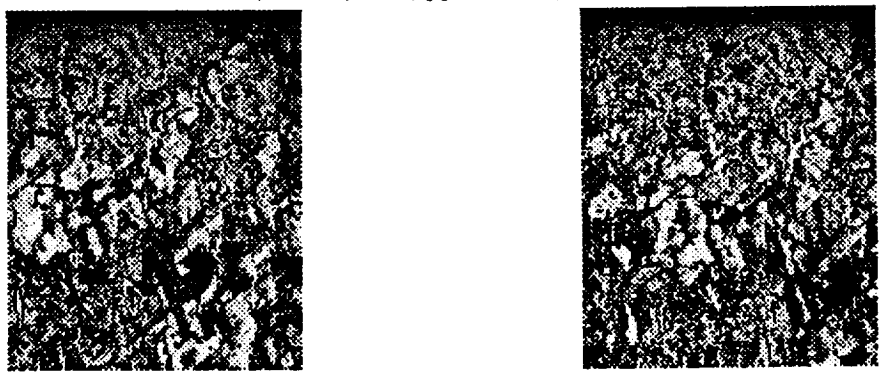

Figure 1. *L-band VV/HH ratio images on June 10 (left) and 18 (right) of study site.*

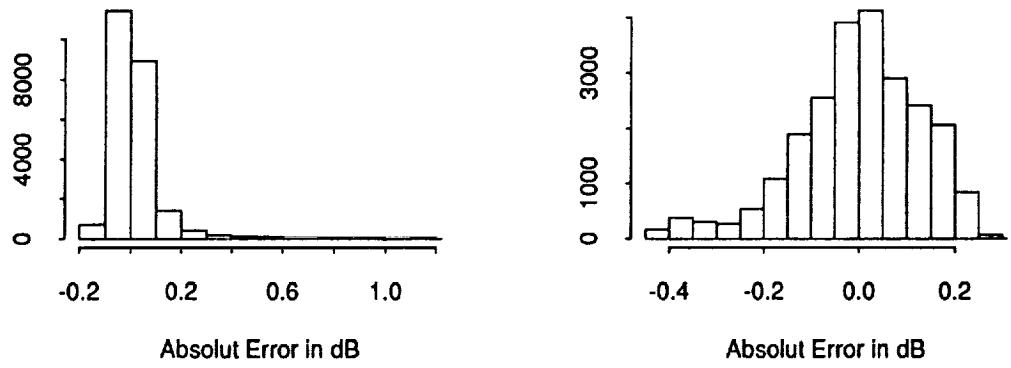

Figure 2. *Comparison the absolute error of the Simplified Model with Integral Equation Model for backscattering coefficients VV on left and HH/VV on right*

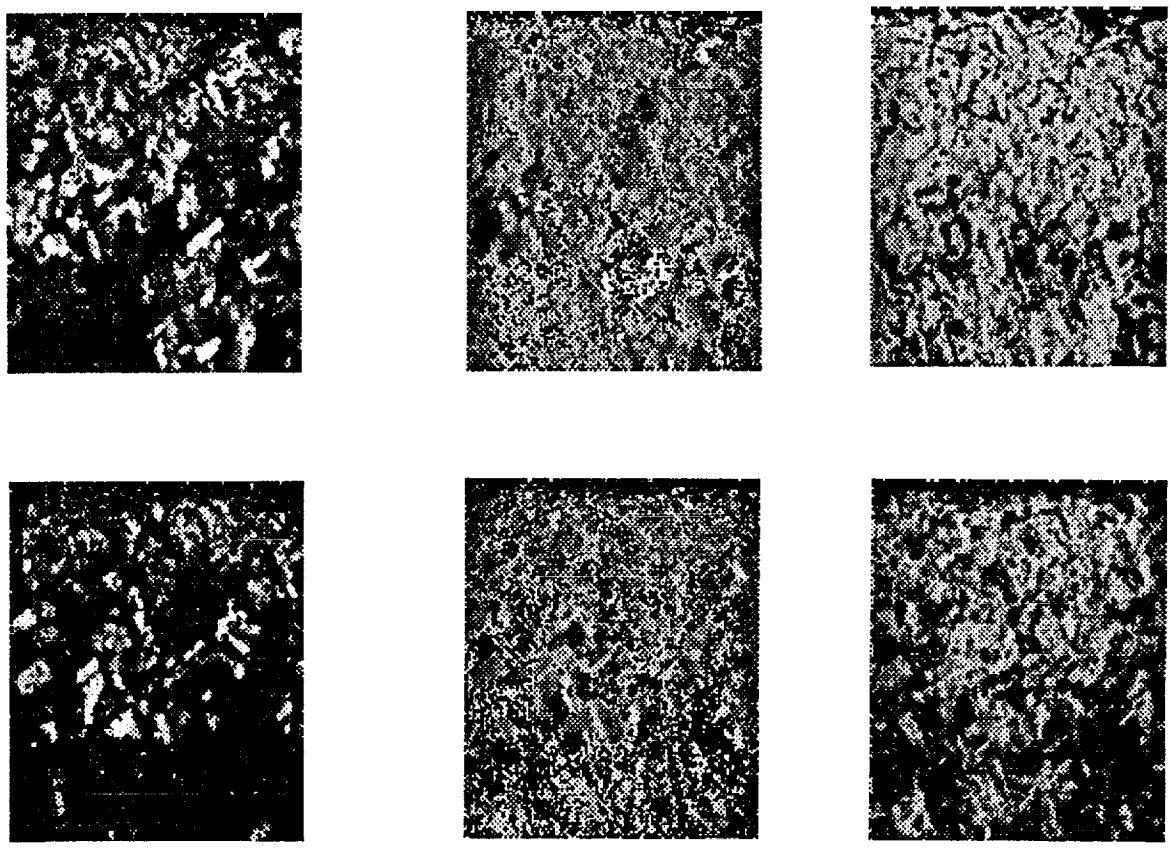

Figure 3 *L-band SAR derived soil moisture and surface roughness parameter maps.*